# A physically-based constitutive model for high temperature microstructural degradation under cyclic deformation

Richard A. Barrett[1,2], Padraic E. O'Donoghue[2,3], Sean B. Leen[1,2]

[1]*Mechanical Engineering, College of Engineering and Informatics, NUI Galway, Galway, Ireland*
[2]*Ryan Institute for Environmental, Marine and Energy Research, NUI Galway, Galway, Ireland*
[3]*Civil Engineering, College of Engineering and Informatics, NUI Galway, Galway, Ireland*

**Corresponding Author:** Richard A. Barrett
**Email:** richard.barrett@nuigalway.ie
**Tel.:** +353 (0) 91 492792

## Abstract

This paper presents a dislocation-mechanics cyclic viscoplasticity model which incorporates the key physical micro-mechanisms of strengthening and softening for high temperature deformation of 9Cr steels. In particular, these include precipitate and grain boundary strengthening, low-angle boundary dislocation annihilation and martensitic lath width evolution, using dislocation density as a key state variable. The new model is applied to P91 steel across a range of strain-rates, strain-ranges and temperatures in the range 400 °C to 600 °C, for power plant header applications, to demonstrate the effect of key microstructural parameters on high temperature low cycle fatigue performance.

## 1. Introduction

The rapid transition in operation of fossil fuel power plants from base-load to flexible loading mode and the drive to higher temperatures, to accommodate renewable energy sources and to reduce $CO_2$ emissions, has led to increased importance of creep, fatigue and oxidation in the design of next generation plant. Advanced materials, such as tempered martensitic-ferritic 9Cr steels, are a common material of choice for heavy section boiler components due to (i) their high creep strength at high temperatures as a result of a precipitate- and solute-strengthened hierarchical microstructure, (ii) their enhanced oxidation and corrosion resistance, primarily due to the relatively high Cr content, (iii) a favourable coefficient of thermal expansion and (iv) relatively low cost compared to other candidate materials, such as Ni-based superalloys. However, due to the diversity and severity of current and future loading conditions, there is a requirement to reliably predict the life of components under more demanding flexible operation at higher temperatures.

1

The microstructure of 9Cr steels is hierarchical in nature, consisting of prior austenite grains, packets, blocks and martensitic laths. This hierarchical microstructure and the key strengthening mechanisms in 9Cr steels are illustrated schematically in Figure 1. Blocks are the smallest region demarcated by high angle grain boundaries (HAGBs) with dislocation substructures of low-angle boundary (LAB) martensitic laths located within the block structures. It is widely documented that the strength of the lath microstructure is inversely proportional to the lath width, $w$, [1,2]. In turn, although not to the same extent as the laths, the HAGB microstructure provides a Hall-Petch type contribution to yield strength, as well as strengthening via the retardation of dislocations and pile-up formation at HAGBs [3]. In the unaged microstructure, two main precipitate types are present; (i) $M_{23}C_6$ carbides dispersed along boundaries and (ii) MX type carbonitrides distributed throughout the microstructure. $M_{23}C_6$ carbides initially have a typical diameter in the region of 50 to 130 nm [1,2], with a volume fraction of approximately 2 % [2]. The nano-scale MX carbonitrides, primarily present in the form of VN and NbC particles, are thermally stable particles with a typical diameter of 10 to 50 nm [2,4-6]. Solid solution strengthening exists predominantly in the form of Mo and W solutes.

High temperature fatigue test programs on 9Cr steels [7-13], typically carried out at high strain-rates (relative to plant operation conditions [13-14]) in the range of 0.01 %/s to 1.0 %/s, exhibited a significant cyclic softening effect. Sauzay and co-workers [15,16] have established that this effect is primarily related to the loss of the lath microstructure and a concomitant reduction in dislocation density. Barrett *et al.* [17,18] showed that a significant strain-rate effect occurs for P91 at 600 °C, although the effect is negligible for temperatures of 500 °C and less. This strain-rate effect has also been observed in other 9Cr martensitic-ferritic steels, such as P92 [11] and MarBN [19], at temperatures in excess of 550 °C.

Under high temperature loading conditions, microstructural degradation is the key contributor to failure. The complex nature of the microstructure, coupled with the harsh loading conditions, results in microstructural evolution in such steels. The mean lath width increases with increasing cycles under high temperature fatigue [11,20], in conjunction with thermal- and strain-dependent coarsening of precipitates [21,22]. Subgrain formation under low cycle fatigue (LCF) has also been observed for a CLAM 9Cr steel at 550 °C [22]. Under creep deformation, the precipitate microstructure also coarsens; new precipitates form at the expense of solutes and the hierarchical lath microstructure transforms to a more equi-axed subgrain dislocation substructure liable to subgrain coarsening, leading (effectively) to a new

microstructure with reduced creep and fatigue performance. This results in a considerable reduction of yield strength and hence, leads to increased plasticity at geometric discontinuities such as weldments, in particular. The role of oxidation is also critical, with the LCF life reduced by at least 50 % in air atmospheres [23] compared with vacuum environments [24] at high temperatures in EUROFER 97, for example. To account for the effects of these complex mechanisms of deformation and microstructural degradation on next generation power plants, effective and efficient material models for constitutive behaviour and life prediction, at the component level, are required.

A wide range of phenomenological models exist for the constitutive behaviour of such materials, including the Chaboche unified cyclic viscoplasticity model [25,26], the two-layer viscoplasticity model [27,28] and the MATMOD model [29]. To predict the strain-rate effect of such materials under high temperature fatigue, a hyperbolic sine modelling methodology was incorporated in a modified Chaboche framework [17,30] and the MATMOD model [29]. The hyperbolic sine formulation represents a more mechanistic approach to defining the inelastic strain-rate [31] and has been successfully applied to a range of materials under creep [32-35] and fatigue [36,37]. For 9Cr steels, Barrett and co-workers [19,30] have shown that the hyperbolic sine function enables reliable interpolation and extrapolation from higher strain-rates in laboratory tests to the intermediate and lower strain-rates relevant to flexible operation of power plants [13].

Although 9Cr steels have a high creep strength, softening due to microstructural degradation remains a key limiting factor for these materials under fatigue. Thus, there is a requirement to predict this microstructural degradation and its effect on the constitutive behaviour. For LCF and thermo-mechanical fatigue of P91 steel, Li *et al.* [38] have recently presented a crystal plasticity (CP) model based on measured EBSD microstructures. However, this meso-scale (block level) model does not incorporate lath and precipitate geometry, although a lath-precipitate micro-mechanical model for P91 for room temperature monotonic behaviour has also been presented [39]. The dislocation-mechanics approach of Giroux and co-workers [11,23] incorporated subgrain width as a key variable for cyclic softening and strengthening in P92 and EUROFER 97 alloys. However, CP can only simulate a very small region and is very time-consuming and computationally intensive for design purposes. Physically-based macro-scale models have been developed for creep: the power law model of Spigarelli [40], the dislocation-mechanics approach of Magnusson and Sandström [41] and the continuum damage mechanics approach of Oruganti *et al.,* [42], for example, have all been applied to

9Cr steels. However, such models do not account for LAB dislocation annihilation and cyclic softening. Sauzay and co-workers [15,16] have developed a theoretical model for the mechanism of cyclic softening in 9Cr steels based on a dislocation-mechanics model for LAB dislocation annihilation. Fournier *et al.* [43] recently developed a self consistent homogenisation model incorporating the LAB dislocation annihilation model of Sauzay and co-workers to predict cyclic softening in a 9Cr alloy at 550 °C, with a kinematic back-stress due to the evolution of the lath microstructure. However, this model omits the key strengthening mechanism provided by the $M_{23}C_6$ and MX precipitates. The previous work of Barrett *et al.* [44] represents an initial step to incorporating precipitate strengthening within a dislocation-mechanics unified cyclic viscoplasticity model. However, this model does not simulate grain boundary (GB) strengthening or lath evolution from a physical basis.

Owing to the hierarchical microstructure of 9Cr steels and the complex interactions of various strengthening mechanisms, a modelling methodology incorporating the complete set of key strengthening mechanisms and evolutions of the microstructure under fatigue at high temperatures is required. The approach presented here accounts for this microstructural degradation via the development of a microstructure-sensitive material model at the macro-scale based on a dislocation-mechanics framework and the evolution of a set of key microstructural parameters. Thus, the focus of the current paper is to extend the work of Barrett *et al.* [44], to modify the hyperbolic sine flow rule to a more physical definition, based on Helmholtz free energy and activation volume, and to include (i) a more physical definition of lath widening, (ii) HAGB strengthening due to the formation of dislocation pile-ups, (iii) an enhanced definition of the precipitate strengthening mechanism accounting for the distribution of carbides along GBs and MX carbonitrides throughout the microstructure and (iv) modelling the evolution of both edge and screw dislocations. This paper also includes application of this model to the evolution of the microstructure under isothermal cyclic (strain-controlled) loading conditions for a P91 steel in the 400 °C to 600 °C temperature range.

## 2. Modelling Methodology

The dislocation-mechanics material model is developed based on a set of key microstructural variables, identified from the primary mechanisms of strengthening in 9Cr steels (e.g. see Figure 1) and the important role they play in cyclic viscoplasticity and creep deformation.

4

This framework is predicated on the evolution and degradation of the material microstructure during cyclic viscoplasticity or creep, such that the inelastic strain-rate is defined as:

$$\dot{\varepsilon}_{in} = f(d_g, w, \lambda, c, \rho), \tag{1}$$

where $d_g$ is block width, $w$ is lath width, $\lambda$ is precipitate spacing, $c$ is the concentration of solutes and $\rho$ is dislocation density.

## 2.1.    A dislocation-mechanics framework for 9Cr steels

At sufficiently large deformation rates, such as in the present paper, diffusional creep mechanisms are insignificant. In this case, the dislocation-mechanics framework is based on the mechanism of dislocation glide, whereby a dislocation will glide (undergo inelastic slip) due to a local thermal activation event [45]. For alloys with obstacles dispersed throughout the microstructure, a mobile dislocation will continue to glide on a given slip plane until it becomes immobilised or annihilated. Under such conditions, the inelastic slip-rate can be defined using Orowan's equation [46]:

$$\dot{\gamma} = \bar{\rho} b v, \tag{2}$$

where $\bar{\rho}$ is mobile dislocation density, $b$ is the magnitude of the Burger's vector (0.248 nm for b.c.c. alloys) and $v$ is the dislocation glide velocity. The inelastic slip-rate can be related to the macro-scale strain-rate via the Taylor model [47]:

$$\dot{\gamma} = \frac{\dot{\varepsilon}_{in} M}{n}, \tag{3}$$

where $M$ is the Taylor factor (2.9 for b.c.c. alloys) and $n$ is the number of active slip systems. The number of active slip systems required to define the deformation-rate in the Taylor model is 5. The glide velocity can be defined in terms of Gibbs Free energy, $\Delta G$, as [48]:

$$v = \bar{A} \exp\left(-\frac{\Delta G}{k_B T}\right), \tag{4}$$

where $\bar{A}$ is a constant, $k_B$ is Boltzmann's constant and $T$ is absolute temperature. The pre-exponential constant, $\bar{A}$, is related to solid solution strengthening mechanisms [49,50] and the frequency factor [31,51,52]. The Gibbs free energy is defined as:

$$\Delta G = \Delta F - \tau_v \Delta V ,\tag{5}$$

where $\Delta F$ is the Helmholtz free energy (the activation energy for dislocation glide in the absence of an applied stress), $\tau_v$ is the viscous shear stress, related to the macroscopic viscous stress, $\sigma_v$, via the Taylor factor ($\sigma_v = M\tau_v$), and $\Delta V$ is activation volume. In Equation (5), the term $\tau_v \Delta V$ represents the work generated by the stress field. Thus, for cyclic deformation, the inelastic strain-rate is defined as:

$$\dot{\varepsilon}_{in} = A \exp\left(\frac{-\Delta F}{k_B T}\right) \sinh\left(\frac{\sigma_v \Delta V}{M k_B T}\right) \text{sgn}(\sigma - \sigma_b),\tag{6}$$

where $A$ is the pre-exponential viscous constant, $\sigma$ is stress and $\sigma_b$ is kinematic back-stress. The use of a hyperbolic sine formulation in Equation (6) allows both forward and backward activation events to be considered [31] and allows for reliable extrapolation and interpolation across a broad range of strain-rates in 9Cr steels due to the mechanistic nature of the hyperbolic sine formulation [30,53]. The kinematic back-stress accounts for long-range dislocation interactions and is incorporated to capture the observed Bauschinger effect in 9Cr steels. As discussed by Keller *et al.* [54], the kinematic back-stress for 9Cr steels consists of partial back-stresses associated with (i) precipitates, (ii) grain boundaries and (iii) dislocation cells. Thus, the kinematic back-stress is defined as:

$$\sigma_b = \sigma_p + \sigma_g + \sigma_w ,\tag{7}$$

where $\sigma_p$ is the back-stress due to particles, $\sigma_g$ is the back-stress due to HAGBs and $\sigma_w$ is the back-stress due to the dislocation substructure. The viscous stress (thermal component of stress) is the difference between the applied stress and the athermal stress components (isotropic and kinematic), defined for uniaxial loading as:

$$\sigma_v = |\sigma - \sigma_b| - \sigma_y^{cyc} ,\tag{8}$$

where $\sigma_y^{cyc}$ is the isotropic cyclic yield stress, defined as:

$$\sigma_y^{cyc} = M(\tau_0 + \tau_d),\tag{9}$$

where $\tau_0$ is the yield stress contribution associated with obstacles such as precipitates, solutes and grain boundaries and $\tau_d$ is the contribution of dislocation density to cyclic yield strength,

quantified using the Taylor hardening equation [55-57], such that the cyclic yield strength can be defined as:

$$\sigma_y^{cyc} = M\left(\tau_0 + \alpha_1 \mu b \sqrt{\rho}\right),$$

(10)

where $\alpha_1$ is a material constant and $\mu$ is shear modulus. As the primary focus of the present study is to predict the effect of the key cyclic softening mechanism (LAB annihilation) on the evolving cyclic yield strength, it is assumed here that $\tau_0$ is a constant, e.g. independent of dislocation density. Thus, the rate change in $\sigma_y^{cyc}$ is:

$$\dot{\sigma}_y^{cyc} = M \frac{\alpha_1 \mu b}{2\sqrt{\rho}} \dot{\rho} .$$

(11)

## 2.2. Precipitate hardening in 9Cr steels

The bowing out of dislocations pinned at precipitates has been observed in TEM studies for both creep and fatigue deformation of 9Cr steels [6,11]. As the dislocation bows out of position between the pinning precipitates, a dislocation annihilation process will occur in a similar manner to that of a Frank-Read source, resulting in dislocation loops being left around the precipitates. The formation of dislocation loops around precipitates in 9Cr steels has been observed in the work of Shrestha *et al.* [58] and Ye *et al.* [59], for example. The kinematic back-stress is a result of the stress field generated by dislocation loops being deposited around precipitates as pinned precipitates bow out of position. This stress field, in turn, increases the resistance to motion for the next dislocation and hence, generates a kinematic back-stress [53]. As pinning of dislocations occurs at both $M_{23}C_6$ and MX precipitates [6], a rule of mixtures approach, similar to that of Magnusson and Sandström [41] and Estrin *et al.* [60], is used to account for the different precipitate microstructures at the boundaries and matrix material (lath interiors), such that the kinematic back-stress is:

$$\sigma_p = \left(f_w + f_g\right)\sigma_{p,BND} + \left(1 - f_w - f_g\right)\sigma_{p,INT},$$

(12)

where $f_w$ and $f_g$ are the volume fractions of the LAB and HAGB regions, respectively, and $\sigma_{p,BND}$ and $\sigma_{p,INT}$ are the precipitate induced kinematic back-stress components at GBs and lath interiors, respectively. An enhanced Fisher-Hart-Pry (FHP) model [61] is developed here to include (i) an inter-particle spacing term more representative of the spacing observed in

9Cr steels, as described in more detail in Appendix A, and (ii) cyclic deformation [44], as well as the kinematic back-stress due to the formation of Orowan loops around precipitates. The modified FHP back-stress is thus defined here as:

$$\sigma_{p,j} = \sigma_{Or,j}\left[1 + 2.48\left(\frac{M\mu K}{\sigma_{Or,j}}\right)^{1/2}f_{j,eq}^{3/4}\left(\frac{\varepsilon_{in}M}{n}\right)^{1/2} + 3.09\frac{M\mu K}{\sigma_{Or,j}}f_{j,eq}^{3/2}\left(\frac{\varepsilon_{in}M}{n}\right)\right], \tag{13}$$

where the subscript j represents different microstructure regions, namely the GB (j = BND, including both LABs and HAGBs) or lath interior (j = INT) regions, $\sigma_{Or,j}$ is the associated Orowan stress, $f_{j,eq}$ is the equivalent associated volume fraction of precipitates in region j and $K$ is a constant, defined as [61]:

$$K = 1 + \frac{1}{2}\left(\frac{v}{1-v}\right), \tag{14}$$

where $v$ is Poisson's ratio. The time evolution of Equation (13) is thus:

$$\dot{\sigma}_{p,j} = \left[1.24M\left(\frac{\sigma_{Or,j}\mu K}{n}\right)^{1/2}\frac{f_{j,eq}^{3/4}}{\sqrt{p_{cyc}}} + 3.09\frac{M^2\mu K}{n}f_{j,eq}^{3/2}\right]\dot{p}\,\mathrm{sgn}(\sigma - \sigma_b), \tag{15}$$

where $\dot{p}$ is the accumulated effective inelastic strain-rate and $p_{cyc}$ is the accumulated effective inelastic strain accumulated during the load reversal. The Orowan stress is defined as:

$$\sigma_{Or,j} = M\phi\frac{\mu b}{\lambda_j}, \tag{16}$$

where $\phi$ is the obstacle strength coefficient and $\lambda_j$ is the mean obstacle spacing. From Figure 1, the mean spacing of obstacles at the GBs and in the lath interiors takes into account the assumption that MX particles are distributed throughout the microstructure and the $M_{23}C_6$ carbides are dispersed along GBs only. Defining the number density of $M_{23}C_6$ and MX particles on the slip plane as $N_c$ and $N_m$, respectively, the total number density of obstacles along the boundary is thus $N_{BND} = N_c + N_m$. Following a similar geometric argument to that of Maruyama $et\ al.$ [1], the mean inter-particle spacing of obstacles is taken as inversely proportional to the square root of the number density of obstacles, $\lambda_j = 1/\sqrt{N_j}$, such that the mean obstacle spacing at the boundaries and within lath interiors are defined as:

8

$$\lambda_{\text{BND}} = \sqrt{\frac{\lambda_c^2 \lambda_m^2}{\lambda_c^2 + \lambda_m^2}}, \tag{17a}$$

$$\lambda_{\text{INT}} = \lambda_m, \tag{17b}$$

where $\lambda_m$ and $\lambda_c$ are the mean inter-particle spacings of the MX carbonitrides and $M_{23}C_6$ carbides, respectively. It is assumed here that excess Mo, i.e. Mo which does not form solutes contributing to solid solution strengthening, forms $Mo_{23}C_6$ carbides dispersed along boundaries. Although the carbides along boundaries are typically dominated by the $Cr_{23}C_6$ carbides, these precipitates are treated here as one family of precipitate and hence, their spacing is quantified using a mean inter-particle spacing approach. A similar approach is taken with the MX carbonitrides, in which the primary precipitate types are NbC and VN particles. The mean inter-particle spacing is defined as [62]:

$$\lambda_k = 1.2 \sqrt{\frac{3}{2}} \frac{r_k}{\sqrt{f_{k,\text{eq}}}} \qquad \text{where k = c, m,} \tag{18}$$

where $r_k$ is particle radius, $f_{k,\text{eq}}$ is the equivalent precipitate volume fraction and the subscripts c and m denote $M_{23}C_6$ carbides and MX carbonitrides, respectively. In Equation (18), the factor 1.2 represents the spacing of a critical pair of precipitates for dislocation pinning [63] and the term $\sqrt{3/2}$ converts the mean square planar radius to the mean square volumetric radius, for evaluation of inter-particle spacing based on the volume fraction of precipitates [61]. In the present work, it is assumed the MX carbonitrides are distributed uniformly throughout the microstructure. Thus, the equivalent volume fraction of MX carbonitrides is the measured volume fraction of particles, i.e. $f_{m,\text{eq}} = f_m$. However, as presented in Figure 1, the $M_{23}C_6$ carbides are assumed to be dispersed along GBs only, such that the equivalent carbide volume fraction is:

$$f_{c,\text{eq}} = \frac{f_c}{f_g + f_w}. \tag{19}$$

9

### 2.3. Back-stress at high-angle grain boundaries

HAGBs retard the motion of dislocations due to the formation of dislocation pile-ups at HAGBs [3,64], as illustrated schematically in Figure 2. This results in a localised back-stress given by [65]:

$$\sigma_g = \frac{Mb\mu}{\alpha_g d_g} n_g \tag{20}$$

where $\alpha_g$ is a material constant with a value of 1/2 and $n_g$ is the number of dislocations in the pile-up. The block size, $d_g$, is used to represent the mean distance between HAGBs. From Equation (20), the evolution of kinematic back-stress due to dislocation pile-ups is:

$$\dot{\sigma}_g = \frac{Mb\mu}{\alpha_g} \left( \frac{d_g \dot{n}_g - n_g \dot{d}_g}{d_g^2} \right) \tag{21}$$

As dislocations of opposite sign can interact at grain boundaries, not all dislocations at the boundaries are available to contribute to the back-stress presented in Equation (21). Hence, the probability that a dislocation contributes to grain boundary strengthening is [66]:

$$P_g = 1 - \frac{n_g}{n_g^*} \tag{22}$$

where $n_g^*$ is the number of sites available for a dislocation to contribute to the dislocation pile-up. Thus, the modified Sinclair model for cyclic deformation of Bardel and co-workers [67] gives:

$$\dot{n}_g = \frac{Ml_g}{b} \left( 1 - \frac{n_g}{n_g^* \operatorname{sgn}(\dot{\varepsilon}_{in})} \right) \dot{\varepsilon}_{in} \tag{23}$$

where $l_g$ is the mean spacing between slip lines and the quantity $l_g/b$ is the number of dislocations required, geometrically, to generate deformation. The block regions do not coarsen significantly under high temperature fatigue and hence, $d_g$ is assumed to remain constant.

## 2.4. Kinematic back-stress due to dislocation substructure

As discussed by Keller *et al.* [54], a back-stress is generated in 9Cr steels due to the existence of a dislocation cell network (martensitic lath LAB dislocation substructure).This back-stress is a function of (i) martensitic lath width, *w*, (ii) angle of misorientation, *θ*, and (iii) density of LAB dislocations, $\rho_w$. The model of Li [68,69], is used to describe the back-stress due to the dislocation substructure as:

$$\sigma_w = \frac{M\mu}{1-v}\sqrt{\frac{0.45\theta b}{2\pi w}} \tag{24}$$

where *v* is Poisson's ratio, *θ* is the angle of misorientation between LABs and *w* is the martensitic lath width. Thus, the rate change in of kinematic back-stress due to the dislocation substructure is:

$$\dot{\sigma}_w = \frac{M\mu}{1-v}\left(\frac{0.45bw}{2\pi\theta}\right)^{1/2}\frac{w\dot{\theta}-\theta\dot{w}}{w^2} \tag{25}$$

## 2.5. Dislocation density evolution

The overall density of dislocations, $\rho$, consists of the mobile dislocation density, $\vec{\rho}$ , and immobile dislocation densities along LABs, HAGBs and within lath interiors, $\rho_w$, $\rho_g$, and $\rho_i$, respectively, such that the overall density of dislocations is:

$$\rho = \vec{\rho} + f_w\rho_w + f_g\rho_g + \left(1 - f_w - f_g\right)\rho_i . \tag{26}$$

The density of dislocations varies as a function of time, due to growth, annihilation and immobilisation processes. The growth of mobile dislocations is assumed to occur due to a Frank-Read source [70], as presented schematically in Figure 3a to Figure 3d. This complex mixed dislocation configuration is modelled here based on the assumption that the Frank-Read source is considered to be made up of edge parts, with a Burgers vector perpendicular to the dislocation line direction and screw parts, characterised by a Burgers vector parallel to the dislocation line direction, as illustrated in Figure 3e. The Orowan equation [46] is used to model the growth of mobile dislocations, assuming that half are of edge type and half of screw type:

$$\dot{\vec{\rho}}_{e}^{+} = \dot{\vec{\rho}}_{s}^{+} = \frac{2}{bL_{\text{eff}}} \frac{\dot{p}M}{n}, \tag{27}$$

where $L_{\text{eff}}$ is the active slip length, the mean free path travelled by a dislocation before it is annihilated or immobilised. The subscripts e and s denote edge and screw type dislocations, respectively, such that the total mobile dislocation density is $\vec{\rho} = \vec{\rho}_{e} + \vec{\rho}_{s}$. For materials with a LAB dislocation substructure, $L_{\text{eff}}$ is approximated as the lath width, $w$ [71].

Consumption of mobile dislocations is attributed (here) to (i) mutual annihilation of mobile dislocations, (ii) LAB dislocation annihilation, (iii) dipole dislocation formation and (iv) formation of locked dislocation configurations.

Mutual annihilation of two mobile dislocations will occur if two edge (or screw) mobile dislocations of opposite sign and anti-parallel Burgers vector are present within a critical area for annihilation (see Figure 4a). Following an approach similar to the work of Roters *et al.* [62] and Hosseini *et al.* [72], two mobile dislocations of opposite Burgers vector and velocity, $v$, will move a total distance of $2v\mathrm{d}t$ towards each other during a time increment, $\mathrm{d}t$, before being annihilated, if both dislocations lie within a critical distance for annihilation, $y_{e}$ for edge (or $y_{s}$ for screw) dislocations. As the annihilation event consumes two mobile edge (or screw) dislocations, the reduction rate of mobile edge (or screw) dislocations is:

$$\dot{\vec{\rho}}_{k}^{-} = 4y_{k} \frac{\dot{p}M}{bn} \frac{\vec{\rho}_{k}^{2}}{\vec{\rho}} \quad \text{where k = e, s.} \tag{28}$$

For edge dislocations, $y_{e}$ is set at a constant value of $6b$ [15,16] and $y_{s}$ is given by the following expression [73]:

$$y_{s} = \frac{\mu b}{2\pi\tau_{\text{crss}}}, \tag{29}$$

where $\tau_{\text{crss}}$ is the critically resolved shear stress, assumed here to be $\tau_{\text{crss}} = \alpha_{1}\mu b\sqrt{\rho}$.

LAB dislocation annihilation follows a similar mechanism to mutual annihilation. However, as LAB dislocations are immobile, only one edge (or screw) mobile dislocation will travel a distance of $v\mathrm{d}t$ to interact with the LAB dislocation within the critical annihilation distance, as illustrated in Figure 4b. Thus, LAB dislocation annihilation occurs when a mobile dislocation of anti-parallel Burger's vector is present within a critical area for annihilation. As

only one edge (or screw) mobile dislocation is annihilated during each event, the contribution to reduction of mobile dislocation density is:

$$\dot{\bar{\rho}}_k^- = y_k \frac{\dot{p}M}{bn} \frac{\vec{\rho}_k \rho_{k,w}}{\bar{\rho}} f_w .$$ (30)

There is a concomitant loss of LAB dislocations, assumed here to be the key mechanism for loss of the LAB structure, such that the decrease in LAB dislocation density is:

$$\dot{\rho}_{w,k}^- = y_k \frac{\dot{p}M}{bn} \frac{\vec{\rho}_k \rho_{k,w}}{\vec{\rho}} .$$ (31)

Dipole dislocations are mobile, but do not accommodate plastic deformation [62,72], and become immobilised on reaching a HAGB. The formation of a dipole configuration is illustrated in Figure 4c for an edge configuration, with the critical distance for dipole generation defined as [72,74,75]:

$$y_{dip} \approx \frac{\sqrt{3}b\mu}{16\pi(1-\nu)\tau_a^*} ,$$ (32)

where $\tau_a^*$ is defined using a Taylor dislocation hardening model as $\alpha_1 \mu b \sqrt{\rho_e + \rho_s}$ . A model similar to that for mutual annihilation can describe the formation of dipole dislocations, such that the rate of reduction in mobile dislocation density is:

$$\dot{\bar{\rho}}_{e-dip}^- = 4 \frac{(y_{dip} - y_e)}{b} \frac{\dot{p}M}{n} \frac{\vec{\rho}_e^2}{\vec{\rho}} .$$ (33)

The generation of screw dipole dislocations is possible [72] but due to the large value of $y_s$, the rate of reaction tends to be quite small and hence, their generation can be neglected.

Locked dislocation configurations can form due to the processes highlighted in Figure 5, leading to the immobilisation of dislocations. As edge-edge (or screw-screw) immobilisation of two mobile dislocations cannot take place on the same slip system, the number of active slip systems in this process is $(n-1)/n$ [72]. Immobilisation via dislocation lock formation in all other processes can occur on all slip systems. Thus, the loss of mobile dislocations due to dislocation lock formation is:

$$\dot{\rho}_{j}^{-} = \frac{y_{l}}{b} \frac{\vec{\rho}_{j}}{\vec{\rho}} \frac{\dot{p}M}{n} \left[ 4(n-1)\vec{\rho}_{j} + 2\vec{\rho}_{k} + \rho_{j} + \rho_{k} \right] \quad \text{where j, k = e, s,} \tag{34}$$

where $y_l$ is the critical distance for locked configurations to form and $\rho_e$ and $\rho_s$ are the density of immobile edge and screw dislocations respectively, defined as:

$$\rho_{j} = (1 - f_{w} - f_{g})\rho_{i,j} + f_{w}\rho_{w,j} + f_{g}\rho_{g,j} \quad \text{where j = e, s.} \tag{35}$$

In the current paper, the evolution of immobile dislocation density only considers LAB dislocation annihilation, the dominant mechanism during cyclic deformation in 9Cr steels. Hence, the densities of immobile dislocations at HAGBs, $\rho_g$, and lath interiors, $\rho_i$, are assumed to remain constant during high temperature LCF.

## 2.6. Modelling the martensitic lath microstructure

Laths (and subgrains) are regions separated by arrays of LAB dislocations with an angle of misorientation of less than 5°. LABs interact with the motion of mobile dislocations due to the high number of boundaries [76], resulting in (i) formation of dislocation entanglements (e.g. locked configurations), (ii) LAB and mobile dislocation annihilation or (iii) Orowan strengthening via the presence of $M_{23}C_6$ carbides dispersed along LABs. The key parameters used here to define the structural integrity of the dislocation substructure are lath (or subgrain) width, shape and angle of misorientation with a neighbouring lath. Hence, to simulate the contribution of the lath structure to the constitutive behaviour of the material, a relationship between the lath width, shape and angle of misorientation is developed. In 9Cr steels, martensitic laths contribute to yield strength [77,78] and control the evolution of dislocation density by defining the mean free path travelled by a dislocation before it is annihilated or consumed [71]. Long-term (creep) transformation of the lath microstructure to a more equi-axed subgrain structure and simultaneous coarsening is not considered here, since the focus is on shorter-term cyclic deformation.

The widening of laths during cyclic loading is defined here as lath coalescence, as the boundary between two adjacent laths does not move but is annihilated to form a single lath configuration. Thus, to simulate cyclic softening of 9Cr steels, i.e. increasing lath width with decreasing LAB dislocation density [15,16], $w$ is defined as [11]:

$$w = \frac{w_0}{1-\kappa} = \frac{w_0 \rho_{w,0}}{\rho_w},$$ (36)

where $\kappa$ is the fraction of annihilated LABs and $w_0$ and $\rho_{w,0}$ are the initial lath width and LAB dislocation density, respectively. The density of LAB dislocations consists of both tilt and twist boundaries, effectively arrays of edge and screw dislocations, respectively [79]. The number of LAB dislocations per metre of boundary, $\Lambda_w$, is [80]:

$$\Lambda_w = \frac{\theta}{b},$$ (37)

where $\theta$ is the angle of misorientation between adjacent laths. The quantity $\Lambda_w$ is converted to dislocation density per unit area via the following process. Assuming that a LAB is only one dislocation wide [81], the LAB dislocation density is:

$$\rho_w = \frac{1}{2} \frac{\Lambda_w P_w}{A_w},$$ (38)

where $P_w$ and $A_w$ are the lath perimeter and lath boundary surface area, respectively, and the factor ½ ensures that a given boundary is only accounted for once. The spacing between two LAB dislocations, $s$, is the reciprocal of $\Lambda_w$. The initial spacing of LAB dislocations defines the width of the LAB region. An idealised lath geometry, based on TEM observations [11,15], is defined in Figure 6. Using this geometry, the perimeter is $4w(X_1+X_2+X_1)$ and the lath boundary surface area is $4s_0\left(w(X_1 + X_2 + X_3) - s_0/2\right)$, such that the density of LAB dislocations is:

$$\rho_w = \frac{1}{2s} \frac{w(X_1 + X_2 + X_3)}{s_0\left(w(X_1 + X_2 + X_3) - \frac{s_0}{2}\right)},$$ (39)

where $s_0$ is initial LAB dislocation spacing (width of LAB) and defined as $b/\theta_0$. Using Equations (37) and (39), the angle of misorientation between adjacent laths is:

$$\theta = \frac{\rho_w b^2 \left[2\theta_0 w(X_1 + X_2 + X_3) - b\right]}{\theta_0^2 w(X_1 + X_2 + X_3)}$$ (40)

Such that the rate change in angle of misorientation between neighbouring laths is defined as:

$$\dot{\theta} = \frac{2b^2}{\theta_0}\dot{\rho}_w - \frac{b^3}{\theta_0^2(X_1 + X_2 + X_3)}\left[\frac{w\dot{\rho}_w - \rho_w\dot{w}}{w^2}\right]$$ (41)

The volume fraction of LABs is also defined using the geometry of Figure 6. Defining the dimensions $L_k = X_k w$, the LAB volume is:

$$V_w = L_1L_2L_3 - (L_1 - s_0)(L_2 - s_0)(L_3 - s_0),$$ (42)

such that the volume fraction of LABs is:

$$f_w = \frac{V_w}{L_1L_2L_3}.$$ (43)

## 3. Identification of material parameters

The proposed material model is applied to a P91 steel tested under strain-controlled conditions at temperatures of 400 to 600 °C. The P91 steel used in this study is an ex-service (ES-P91) material extracted from a power plant after 36,168 hrs service and 65 start-up and shut-down cycles. Although ex-service, the material was only subjected to subcritical conditions below 485 °C when in service and was removed from service for operational reasons only. Hence, it is assumed that the ES-P91 material has negligible microstructural degradation and minimal creep damage and is comparable to an 'as received' P91 alloy. The chemical composition of the P91 steel is presented in Table 1. The material underwent a two stage heat treatment process of normalisation for 0.5 hrs at 1050 °C followed by tempering at 765 °C for 1 hr prior to service.

Figure 7 illustrates a flowchart for implementation of the uniaxial set of equations in a non-linear solution scheme. The identification process for material parameters follows a step-by-step methodology, with the majority of material parameters identified using mechanistic approaches and physical values. The primary steps in this process are identification of the (i) elastic, (ii) viscous, (iii) precipitate and solute, (iv) HAGB strengthening and hierarchical microstructure and (v) dislocation density material parameters.

### 3.1. Cottrell's stress partitioning method and identification of the elastic constants

The temperature-dependent Young's modulus, $E$, is identified from the slope of the initial elastic region of the first cycle and Poisson's ratio, $v$, is assumed to be 0.3 throughout.

Cottrell's stress partitioning method [82] is employed to define the initial cyclic yield stress, $\sigma_{y,0}^{cyc}$, and the evolution of the cyclic yield stress via consideration of the stress response during a dwell test and determination of the thermal and athermal components of stress. Figure 8 depicts application of Cottrell's method to the initial cycle for the P91 steel of the current study at a temperature of 600 °C with a dwell period of 120 s. From Figure 8, the cyclic yield stress, $\sigma_y^{cyc}$, and the kinematic back-stress, $\sigma_b$, are defined as:

$$\sigma_y^{cyc} = \frac{\sigma_{max} - \sigma_v - \sigma_r}{2},$$ (44a)

$$\sigma_b = \frac{\sigma_{max} + \sigma_v - \sigma_r}{2},$$ (44b)

where $\sigma_{max}$ is the maximum stress (point B) and $\sigma_r$ is the reversal yield stress (point D) for the initial cyclic. The temperature-dependent Young's modulus and initial cyclic yield stress are presented in Table 2.

### 3.2. Determination of viscous constants and activation volume from dwell tests

The pre-exponential viscous constant, $A$, Helmholtz free energy, $\Delta F$, and activation volume, $\Delta V$, are identified from stress relaxation test data. The activation volume can be defined in terms of the temperature-dependent engineering strain-rate sensitivity parameter, $m(T)$ [83]:

$$\Delta V = \frac{M k_B T}{m(T) \sigma}.$$ (45)

At higher applied strain-rates, the hyperbolic sine constitutive formulation of Equation (6) can be replaced by an exponential equation of the form:

$$\dot{\varepsilon}_{in} = A \exp\left(\frac{-\Delta F}{k_B T}\right) \exp\left(\frac{\sigma_v}{m(T)\sigma}\right) \mathrm{sgn}(\sigma - \sigma_b) = \alpha(T) \exp\left(\frac{\sigma_v}{m(T)\sigma}\right) \mathrm{sgn}(\sigma - \sigma_b)$$ (46)

where $\alpha(T)$ is the temperature-dependent viscous constant. The required parameters, $\alpha(T)$ and $m(T)$, are identified by defining the inelastic strain-rate, $\dot{\varepsilon}_{in}$, stress, $\sigma$, and viscous stress, $\sigma_v$, at discrete points along the hold period of a stress relaxation test, as described in Appendix B. The identified temperature-dependent constants for $\alpha(T)$ and $m(T)$ are presented in Figure 9, with the identified values of $m(T)$ using this fitting procedure in close agreement with values

for 9Cr steels presented in the literature [84]. From Equation (46), the natural logarithm of $\alpha(T)$ is:

$$\ln(\alpha) = \ln(A) - \frac{\Delta F}{k_B T}.$$  (47)

Thus, plotting $\ln(\alpha)$ against $1/T$ allows for the determination of the Helmholtz free energy, $\Delta F$, and pre-exponential viscous constant, $A$, from the slope and intercept, respectively. For the P91 alloy of the present study, this is illustrated in Figure 10, where the identified $\Delta F$ value of $5.95 \times 10^{-19}$ J (corresponding to a thermal activation energy of 358.4 J/mol.K) is in good agreement with published values [42].

### 3.3.    Precipitate strengthening material parameters

The parameters related to the precipitate induced kinematic back-stress are precipitate radius, $r_k$, volume fraction, $f_k$, and the obstacle strength coefficient, $\phi$. For cyclic loading at higher applied strain-rates, it is assumed here that $r_k$ and $f_k$ remain constant. The mean radii and volume fractions of the $M_{23}C_6$ carbides and MX carbonitrides are obtained from the work of Abe [2], as presented in Table 3. The Orowan stresses and mean obstacle spacing related to $M_{23}C_6$ and MX particles are determined using Equations (16) and (18), respectively, as presented in Table 3. These values are consistent with previously reported values by Abe [2]. From the work of Ijiri *et al.* [85], the obstacle strength coefficient is in the range of 0.59 to 0.8, with a value of 0.6 corresponding to the predicted spacing values presented in Table 3.

### 3.4.    HAGB strengthening and hierarchical microstructure constants

Once the precipitate strengthening parameters have been identified, the HAGB strengthening parameters of $n_g^*$ and $l_g$ are fitted to experimental data, ensuring good correlation with (i) kinematic back-stress as identified from Figure 8 and (ii) stress-strain data under the calibration conditions. From this fitting procedure, the constant $n_g^*$ is assumed to have temperature-dependence to obtain a best fit with experimental data. The identified temperature-dependent constant, $n_g^*$, is found to be proportional to the ratio of the shear modulus at the current temperature to the shear modulus at room temperature raised to the power of ½ (i.e. $(\mu_0/\mu)^{1/2}$). The justification for a temperature-dependent $n_g^*$ is based on the assumption that the energy required for a dislocation to penetrate a HAGB is reduced at

higher temperatures, i.e. the critical stress for penetration of the HAGB by the lead dislocation in the pile-up is reduced with increasing temperature.

The grain size parameters of $d_g$, $w_0$ and $\theta_0$ are identified from published data [16,86] and EBSD measurements [87]. The identified values of $d_g$, $w_0$ and $\theta_0$ are 4.0 μm, 0.4 μm and 1.96°, respectively, consistent with previously-reported data typical ranges for P91 alloys, e.g. [1,2,4,6,86].

### 3.5. Identification of dislocation density material constants

The required dislocation density parameters are determined from previously published microstructural data. The initial mobile dislocation density, $\bar{\rho}$, is taken as $1.6 \times 10^{14}$ m$^{-2}$, utilising the TEM measurements by Sauzay and co-workers [15,16]. Based on the idealised geometry of Figure 6, with $X_1=4.0$ and $X_2=X_3=1.0$, the initial LAB dislocation density, $\rho_{w,0}$, is found to be $9.52 \times 10^{15}$ m$^{-2}$ (using Equation (39)), which is consistent with the findings of Magnusson and Sandström [41]. The density of HAGB dislocations is assigned a value of $10^{15}$ m$^{-2}$. Assuming that the boundary region width is the product of $n_g^*$ and the mean spacing of HAGB dislocations, determined as $s_g = 1/\sqrt{\rho_g}$, $f_g$ is given by:

$$f_g = 1 - \frac{\left(Y_1 d_g - n_g^*/\sqrt{\rho_g}\right)\left(Y_2 d_g - n_g^*/\sqrt{\rho_g}\right)\left(Y_3 d_g - n_g^*/\sqrt{\rho_g}\right)}{Y_1 Y_2 Y_3 d_g^3} \tag{48}$$

where $Y_k$ (k = 1 to 3) are the characteristic lengths of the block geometry (similar to $X_k$ of Figure 6). It is assumed here that the blocks are equi-axed, i.e. $Y_k = 1.0$. The initial density of the lath interior immobile dislocations, $\rho_{i,0}$, is assigned a value of $1.0 \times 10^{11}$ m$^{-2}$, based on the assumption that the material is initially in a relaxed state [41]. The final unknown parameter in the dislocation density evolution equations, $y_l$, is identified as $b$ using a best fit to experimental data for cyclic softening, and is consistent with previous work [62,72]. The complete set of temperature-independent material parameters are presented in Table 4.

## 4. Results and discussion

### 4.1. Comparison with LCF data

Figure 11 presents the model predicted stress-strain comparison with experimental data for the calibration conditions of a strain-rate of 0.1 %/s and applied strain-range of ±0.5 %. Close agreement is obtained with the experimental data in general, particularly for the effects of cyclic softening, a key aspect of the present work. The comparison with stress relaxation presented in Figure 12 is also reasonably close across all temperatures, highlighting the importance of the physically-based hyperbolic sine approach used in the current study. The ability of the model to predict the evolution of maximum and cyclic yield stress is presented in Figure 13, where good agreement with the data is obtained for temperatures of 400 °C and 600 °C. The results of Figure 13 reflect the ability of the dislocation-mechanics modelling framework, controlled by the evolution of martensitic lath width, to capture the cyclic softening behaviour in 9Cr steels.

The model is validated against P91 test data for a range of strain-rates and strain-ranges distinct from the calibration conditions. The results are presented in Figure 14 for the initial and softened states across multiple strain ranges at a temperature of 400 °C, with results of similar quality obtained at 500 °C and 600 °C. Figure 15 compares the predicted stress-strain response at strain-rates of 0.033 %/s and 0.025 %/s for the initial and 600th cycles. Figure 16 shows the predicted athermal (kinematic back-stress and cyclic yield stress) and thermal (viscous) components of stress for the initial and 300th cycles at 600 °C. The large component of viscous stress is consistent with the large reduction in stress during a dwell period at 600 °C (e.g. see Figure 12a).

### 4.2. Prediction of microstructural evolution under cyclic loading in 9Cr steels

The effects of cyclic loading on the evolution of microstructural parameters, such as lath width and mobile dislocation density, are also investigated, including comparisons against the rather limited microstructural data available for cyclic deformation. Figure 17a shows a comparison of the predicted evolution of lath width, with measured data [16,86] for a temperature of 600 °C. The predicted values show significantly more growth than the measured data of Hyde *et al.* [86], although there is very good agreement between the model and the final measured value of 1.5 μm when compared with the data of Sauzay *et al.* [16].

The evolution of mobile dislocation density is presented in Figure 17b; the final predicted value is in close agreement with that of Sauzay *et al.* [16], highlighting the ability of the material model to predict the evolution of mobile dislocation density. The initial loss of mobile dislocations for 600 °C (i.e. during cycle 1), is quite large. This may be attributable to the choice of the parameter, $y_l$, and the omission of immobile dislocation density evolution, although a rapid initial decrease of dislocation density has been observed for the creep deformation of 9Cr steels [88]. Figure 18 shows the predicted effect of initial lath width on evolutions of LAB and mobile dislocation densities. Although a significantly higher LAB dislocation density is predicted throughout, the key effect is the more sizeable reduction of mobile dislocation density for the coarser lath case, illustrating the benefits of a fine initial lath microstructure.

The small effect of temperature on the cyclic evolution of lath width (as predicted in Figure 19a) is expected due to the small effect of thermal aging on lath widening at temperatures of 600 °C or less [89]. This highlights the importance of plastic deformation on the LAB dislocation annihilation process under flexible power plant operating conditions. Note that the cross slip mechanism for immobile dislocations has been omitted from the present study, assuming that dislocation glide is the dominant mechanism for dislocation annihilation. Figure 19b shows the predicted effect of temperature on the dislocation density evolution for temperatures of 400 °C, 500 °C and 600 °C. An overall trend of a loss of mobile dislocations is predicted, consistent with experimental observations [11,15,16] and indicative of cyclic softening. A higher rate of mobile dislocation density reduction and hence, a higher rate of cyclic softening, is predicted at a temperature of 600 °C, consistent with experimental data.

### 4.3. Effect of key microstructure parameters on constitutive behaviour

This section describes the results of a sensitivity study of the effect of key microstructural parameters on the constitutive behaviour of P91 steel using the validated model, including the effect of precipitate diameter and volume fraction, lath shape, and the effect of initial block size. These microstructural parameters, which are sensitive to the heat treatment process and thermal aging, directly affect the key strengthening mechanisms for both fatigue and creep loading, and hence, play an important role in the high temperature performance of P91 steel. The predictions are discussed in relation to the plastic strain-range, a key variable in many fatigue damage models [90] and it should be noted that this type of microstructural study is difficult to conduct experimentally.

21

The predicted effects of (initial) radii of MX and $M_{23}C_6$ precipitates on the hysteresis loop for the 1000th cycle at 600 °C are shown in Figure 20. Smaller precipitates (for a constant volume fraction) are seen to give a material of higher strength as expected, due to the increased number of obstacles to impede dislocation motion. The predicted effect of precipitate volume fraction is illustrated in Figure 21, demonstrating that an increased volume fraction of precipitates causes a harder response due to decreased mean inter-particle spacing. The predicted changes in plastic strain-range are of the order of 5 % for MX carbonitrides and 7 % for $M_{23}C_6$ carbides, for both particle radii and volume fraction investigations.

The initial block size of 9Cr steels is dependent on the heat treatment process and longer hold times and higher temperatures result in a coarser microstructure. In the model developed here, the effect of block size is taken into account via the back-stress for dislocations accumulating at HAGBs (see Equation (21)). The model predicts that coarser microstructures give a softer response (reduced stress-range), as illustrated by the result presented in Figure 22. The decrease in stress-range for increasing initial block width gives an increased plastic strain-range for strain-controlled loading conditions. This, in turn, can be expected to reduce LCF life, assuming that strain-life response is independent of block width and highlights the requirement to optimise heat treatment for creep-fatigue loading conditions.

Martensitic laths are commonly considered to be the key source of high strength in 9-12Cr steels. In the current work, it is assumed that martensitic lath width controls the evolution of dislocation density by (i) LAB dislocation annihilation, (ii) representing the physical length-scale for the mean free path of a mobile dislocation before it is annihilated or consumed [71] and (iii) quantifying the volume fraction of LABs. The effect of lath shape on the constitutive behaviour and predicted plastic-strain range for the 1000th cycle, at a temperature of 600 °C, is presented in Figure 23a. The lath shapes investigated have geometric coefficients of $X_k$ = (4,4,1), $X_k$ = (4,4,1), corresponding to elongated laths and $X_k$ = (1,1,1) corresponding to more equi-axed subgrains, similar to the subgrain model of Giroux [11]. For an applied strain-range of ±0.3 %, a 19 % increase in plastic strain range is observed for the (1,1,1) equi-axed subgrain structure when compared to the case with geometric coefficients of (4,4,1). This significant increase in plastic strain-range results in increased LAB coarsening and hence, a higher rate of cyclic softening, as illustrated in Figure 23b. The results of Figure 23 highlight the importance of the initial lath microstructure on the cyclic plasticity fatigue performance of 9Cr steels. It is concluded here that it is key to mitigate subgrain formation during heat treatment, welding and creep deformation. Subgrains form due to over-tempered martensite

22

[88,91] or via creep-fatigue deformation with martensitic lath to subgrain transformation [54].

From the present microstructural evolution predictions and comparisons with measured microstructural data from the literature, it is clear that cyclic deformation can have a detrimental effect on structural integrity of P91 and similar materials. In particular, the initial rapid decrease of dislocation density, concomitant with a rapid increase in lath width, leads to a much coarser microstructure over a relatively small number of cycles. This coarser hierarchical microstructure results in a material with a significantly reduced creep strength. This highlights the requirement for modelling of material microstructure evolution in fatigue-creep and creep-fatigue studies and design. Due to the potential short time to fatigue crack initiation in 9Cr steels [90], the effects of the formation of micro-cracks at point defects such as $M_{23}C_6$ and MX precipitates cannot be omitted and this can be exacerbated at high temperatures by their potential contribution to the coalescence of creep voids along boundaries. This motivates the inclusion of HAGBs and dislocation pile-up formation in a microstructure-sensitive macro-scale material model [5].

## 5. Conclusions

This paper presents a dislocation-mechanics unified cyclic viscoplastic constitutive model for 9Cr steels. The model incorporates the key microstructural parameters within a strain-rate sensitive framework, including a physically-based kinematic back-stress incorporating the effects of (i) $M_{23}C_6$ and MX precipitate strengthening and (ii) formation of dislocation pile-ups at high-angle grain boundaries, and dislocation density based cyclic softening. The key conclusions are:

- The initial martensitic lath width is predicted to control the degree of cyclic softening.
- Martensitic lath coalescence due to the loss of the low-angle boundary microstructure is predicted to be severe for initial cycles. This is anticipated to have a significant effect on thermo-mechanical performance.
- There is a requirement for long-term thermal (and strain-dependent) stability of precipitates and it is important to maintain a minimum block width during heat treatment, within the hierarchical microstructure, for high temperature cyclic deformation.
- The microstructural model is capable of predicting the strain-rate effect via the variable strain-rate sensitivity of the hyperbolic sine formulation.

- Due to the complex hierarchical microstructure of 9Cr steels, it is important to represent the multiple physically-based strengthening and softening mechanisms to accurately predict the effects of heat treatment and thermo-mechanical phenomena on constitutive behaviour.

- Materials with an equi-axed subgrain microstructure are predicted to have a higher rate of cyclic softening compared to a martensitic lath microstructure.

# Nomenclature

| Parameter | Symbol | Parameter | Symbol |
|---|---|---|---|
| Pre-exponential constant | $A$ | Taylor hardening coefficient | $\alpha_1$ |
| Magnitude of Burger's vector | $b$ | GB material constant | $\alpha_g$ |
| Solute strengthening coefficient | $B$ | Inelastic slip | $\gamma$ |
| Solute concentration | $c$ | Inelastic strain | $\varepsilon_{in}$ |
| Block width | $d_g$ | Helmholtz free energy | $\Delta F$ |
| HAGB volume fraction | $f_g$ | Gibbs free energy | $\Delta G$ |
| Precipitate volume fraction | $f_k$ | Activation volume | $\Delta V$ |
| LAB volume fraction | $f_w$ | Lath angle of misorientation | $\theta$ |
| Material constant | $K$ | Fraction of LABs annihilated | $\kappa$ |
| Boltzmann constant | $k_B$ | Inter-particle spacing | $\lambda$ |
| Mean spacing between slip lines | $l_g$ | LAB dislocations per metre | $\Lambda_w$ |
| Dislocation mean free path | $L_{eff}$ | Shear modulus | $\mu$ |
| Strain-rate sensitivity parameter | $m$ | Poisson's ratio | $v$ |
| Taylor factor | $M$ | Mobile dislocation density | $\vec{\rho}$ |
| Number of active slip systems | $n$ | HAGB immobile dislocation density | $\rho_g$ |
| Number of sites for dislocation pile-ups | $n_g$ | Lath interior immobile dislocation density | $\rho_i$ |
| Number density of precipitates | $N_j$ | Applied stress | $\sigma$ |
| Accumulated effective inelastic strain | $p$ | Kinematic back-stress | $\sigma_b$ |
| Accumulated effective inelastic strain during load reversal | $p_{cyc}$ | Dislocation pile-up back-stress | $\sigma_g$ |
| Precipitate radius | $r_k$ | Orowan stress | $\sigma_{Or}$ |
| Dislocation spacing | $s_k$ | Precipitate back-stress | $\sigma_p$ |
| Absolute temperature | $T$ | Dislocation substructure back-stress | $\sigma_w$ |
| Dislocation line tension | $T_L$ | Viscous stress | $\sigma_v$ |
| Dislocation glide velocity | $v$ | Cyclic yield stress | $\sigma_y^{cyc}$ |
| Lath width | $w$ | Shear stress | $\tau$ |
| Lath characteristic length coefficient | $X_k$ | Friction shear stress | $\tau_0$ |
| Block characteristic length coefficient | $Y_k$ | Dislocation shear stress | $\tau_d$ |
| Critical annihilation distance | $y_k$ | Solute shear stress | $\tau_{ss}$ |
| Critical distance for formation of dislocation locks | $y_l$ | Viscous shear stress | $\tau_v$ |
| Viscous stress constant | $\alpha$ | Obstacle strength coefficient | $\phi$ |

**Appendix A: Derivation of the modified FHP model for cyclic deformation of 9Cr steels**

Considering the dislocation pinned at two particles in Figure 24 and bowing out of position under an applied shear stress, $\tau$, equilibrium of forces at an arbitrary point P along the bowed out dislocation gives:

$$T_{\mathrm{L}} = (\tau - \tau_{\mathrm{m}})bR \tag{A1}$$

where $T_{\mathrm{L}}$ is the dislocation line tension, $R$ is the radius of curvature of the bowed dislocation and $\tau_{\mathrm{m}}$ is the stress due to both particles, defined as [61]:

$$\tau_{\mathrm{m}} = \tau_{\mathrm{m},1} + \tau_{\mathrm{m},2} = K\left(\frac{\mu b}{4\pi}\right)\sum_{i=1}^{2}\frac{N_{\mathrm{i}}}{R_{\mathrm{i}}^3}\pi r_{\mathrm{s},i}^2 \tag{A2}$$

where $N_{\mathrm{i}}$ and $r_{\mathrm{s},i}$ are the number of loops around and mean square planar radius of particle i, respectively, and $R_{\mathrm{i}}$ is the distance from particle i to the arbitrary point P of the bowed out dislocation. Thus, normalising Equation (A1) with respect to the Orowan stress, $\tau_{\mathrm{Or}}$, the equilibrium condition becomes:

$$\frac{\lambda}{2R} = \frac{\tau}{\tau_{\mathrm{Or}}} - \sum_{i=1}^{2}\frac{\varphi_{\mathrm{i}}}{\chi_{\mathrm{i}}^3} \tag{A3}$$

where $\chi_i$ is $2R_{\mathrm{i}}/\lambda$ and:

$$\varphi_{\mathrm{i}} = 2KN_{\mathrm{i}}\frac{r_{\mathrm{s},i}^2}{\lambda^2} \tag{A4}$$

It is assumed here that all particles are spherical in shape with equal dimensions, and hence, provide equal strength across all slip planes. Furthermore, due to this assumption of uniform distribution and size, the number of dislocation loops around any two arbitrary particles will be equal. Thus, following the work of Hart [61], an empirical solution to Equation (A3) is:

$$\frac{\tau}{\tau_{\mathrm{Or}}} = 1 + 2\varphi^{1/2} + 2\varphi \tag{A5}$$

The number of dislocation loops, $N$, around a given particle can be related to glide strain as [61,92]:

$$N = \frac{2r_{\mathrm{v}}}{b}\gamma_{\mathrm{in}} \tag{A6}$$

where $r_{\mathrm{v}}$ is the mean volumetric radius of the particle and $\gamma_{\mathrm{in}}$ is inelastic slip. The mean volumetric radius is related to the mean square planar radius as [61]:

$$r_{\mathrm{v}} = \sqrt{\frac{3}{2}} r_{\mathrm{s}}$$  (A7)

If the distance between a critical pair of particles is $1.2l$, where $l$ is the mean spacing between particles, then the critical mean inter-particle spacing is defined as:

$$\lambda = 1.2 \frac{r_{\mathrm{v}}}{\sqrt{f}}$$  (A8)

where $f$ is the volume fraction of particles. Thus, the term $\varphi$ becomes:

$$\varphi_{\mathrm{i}} = \frac{8}{3} \frac{\mu K}{\tau_{\mathrm{Or}}} \frac{r_{\mathrm{v}}^3}{\lambda^3} \gamma_{\mathrm{in}} = 1.54 \frac{\mu K}{\tau_{\mathrm{Or}}} f^{3/2} \gamma_{\mathrm{in}}$$  (A9)

and the back-stress term is:

$$\tau = \tau_{\mathrm{Or}} \left[ 1 + 2.48 \left( \frac{\mu K}{\tau_{\mathrm{Or}}} \right)^{1/2} f^{3/4} \left( \gamma_{\mathrm{in}} \right)^{1/2} + 3.08 \frac{\mu K}{\tau_{\mathrm{Or}}} f^{3/2} \gamma_{\mathrm{in}} \right]$$  (A10)

Using the Taylor model to convert to the macro-scale yields:

$$\sigma_{\mathrm{p}} = \sigma_{\mathrm{Or}} \left[ 1 + 2.48 \left( \frac{M \mu K}{\sigma_{\mathrm{Or}}} \right)^{1/2} f^{3/4} \left( \frac{\varepsilon_{\mathrm{in}} M}{n} \right)^{1/2} + 3.09 \frac{M \mu K}{\sigma_{\mathrm{Or}}} f^{3/2} \frac{\varepsilon_{\mathrm{in}} M}{n} \right]$$  (A11)

**Appendix B: Estimation of the inelastic strain-rates under stress-relaxation conditions**

The inelastic strain-rate and viscous stress during stress relaxation are identified using the following process. In the present work, it is assumed that $\sigma_{\mathrm{v}}$ relaxes during the dwell period from a maximum value at $t_0$ (point B), to a minimum value of approximately zero at point C (see Figure 8). To omit the effects of experimental noise during the calculation of the time derivative of inelastic strain, the stress during a dwell period is redefined using a polynomial fit as a function of $\log(t)$:

$$\sigma = a_0 + a_1 \log(t) + a_2 \left[ \log(t) \right]^2 + a_3 \left[ \log(t) \right]^3,$$  (B1)

where $a_{\mathrm{i}}$ are the constants of the polynomial and $t$ is time. Equation (B1) is similar to the expression of Takahashi [93], with the final term added to give an improved fit during the initial stages of stress relaxation. Applying Hooke's law and taking a time derivative gives the inelastic strain-rate as:

$$\dot{\varepsilon}_{\mathrm{in}} = - \frac{\left( a_1 + 2a_2 \left[ \log(t) \right] + 3a_3 \left[ \log(t) \right]^2 \right)}{Et \ln(10)}.$$  (B2)

As the fit of stress is not well defined at $t_0$, the inelastic strain-rate at $t_0$ is defined by fitting a polynomial of $t$ for the hardening region of the monotonic curve, such that the stress and inelastic strain-rate are defined as:

$$\sigma = b_0 + b_1 t + b_2 t^2 + b_3 t^3 , \tag{B3}$$

$$\dot{\varepsilon}_{in} = \dot{\varepsilon} - \frac{\left( b_1 + 2b_2 t + 3b_3 t^2 \right)}{E} , \tag{B4}$$

where $b_i$ are the polynomial constants for the monotonic hardening region.

**Acknowledgements**

## Tables

Table 1: Chemical composition of the ES-P91 steel in wt%. The balance Fe.

| Al | C | Cr | Mn | Mo | N | Nb | Ni | P | Si | V |
|---|---|---|---|---|---|---|---|---|---|---|
| 0.007 | 0.1 | 8.48 | 0.42 | 0.94 | 0.058 | 0.073 | 0.19 | 0.013 | 0.26 | 0.204 |

Table 2: Temperature-dependent material parameters.

| $T$ (°C) | $E$ (GPa) | $\sigma_{y,0}^{cyc}$ (MPa) | $m$ (-) | $n_g^*$ (-) |
|---|---|---|---|---|
| 400 | 185 | 190.7 | 0.014 | 15.6 |
| 500 | 165 | 154.3 | 0.027 | 12.1 |
| 600 | 139 | 108.1 | 0.082 | 8.82 |

Table 3: $M_{23}C_6$ and MX precipitate parameters for P91. The Orowan stress is calculated at room temperature, with a shear modulus of 90 GPa.

| Particle | Radius [2] | Volume fraction [2] | Spacing (Eq. 18) | Orowan stress (Eq. 16) |
|---|---|---|---|---|
| $M_{23}C_6$ | 25 nm | 2.0 % | 259.8 nm | 149.9 MPa |
| MX | 10 nm | 0.2 % | 328.6 nm | 118.2 MPa |

Table 4: Temperature-independent material parameters for 9Cr steel.

| Parameter | Symbol | Value | Source |
|---|---|---|---|
| Pre-exponential constant | $A$ | $1 \times 10^{16}$ s$^{-1}$ | Present work |
| Block width | $d_g$ | 4.0 μm | SEM [16] |
| Mean spacing between slip lines | $l_g$ | 300 nm | Present work |
| Initial lath width | $w_0$ | 400 nm | EBSD, TEM [87] |
| Lath characteristic length coefficients | $X_1, X_2, X_3$ | 4, 1, 1 | Assumed |
| Block characteristic length coefficients | $Y_1, Y_2, Y_3$ | 1, 1, 1 | Assumed |
| Critical annihilation distance for edge dislocations | $y_e$ | $6b$ nm | [15,16] |
| Critical distance for formation of dislocation locks | $y_l$ | $b$ nm | Present work |
| Taylor hardening coefficient | $\alpha_1$ | 0.2 | Assumed |
| Helmholtz free energy | $\Delta F$ | $5.95 \times 10^{-19}$ J | Present work |
| Initial lath angle of misorientation | $\theta_0$ | 1.96° | EBSD [87] |
| Obstacle strength coefficient | $\phi$ | 0.7 | [85] |
| Poisson's ratio | $v$ | 0.3 | Assumed |
| Initial mobile dislocation density | $\vec{\rho}_o$ | $1.6 \times 10^{14}$ m$^{-2}$ | TEM [16] |
| HAGB immobile dislocation density | $\rho_g$ | $1.0 \times 10^{15}$ m$^{-2}$ | [41] |
| Lath interior immobile dislocation density | $\rho_i$ | $1.0 \times 10^{11}$ m$^{-2}$ | [41] |

**Figures**
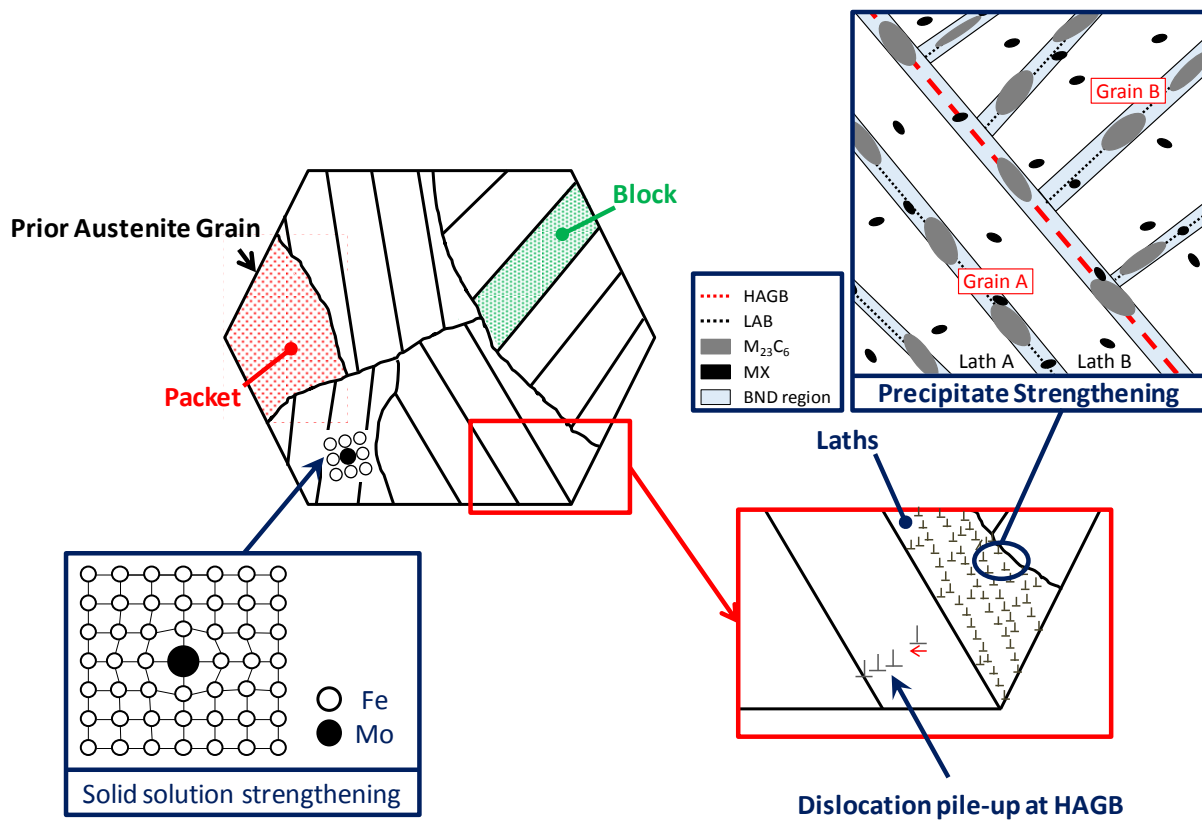


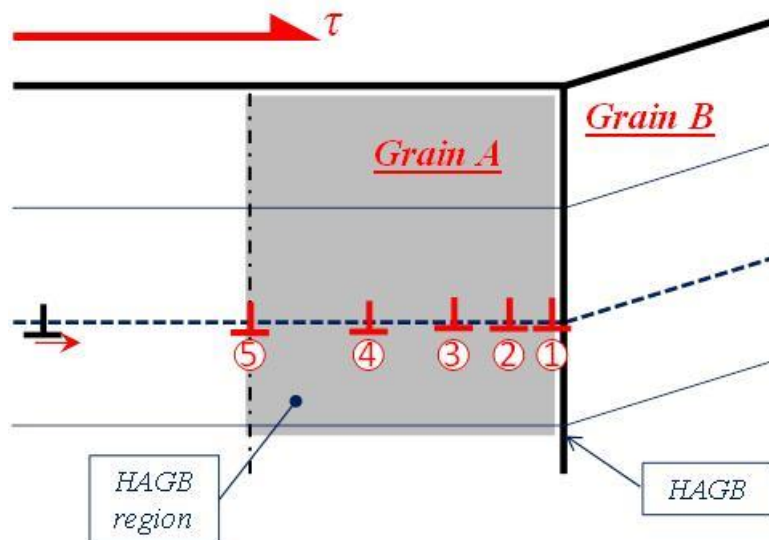Figure 1: Hierarchical microstructure and key strengthening mechanisms in 9-12Cr steels.



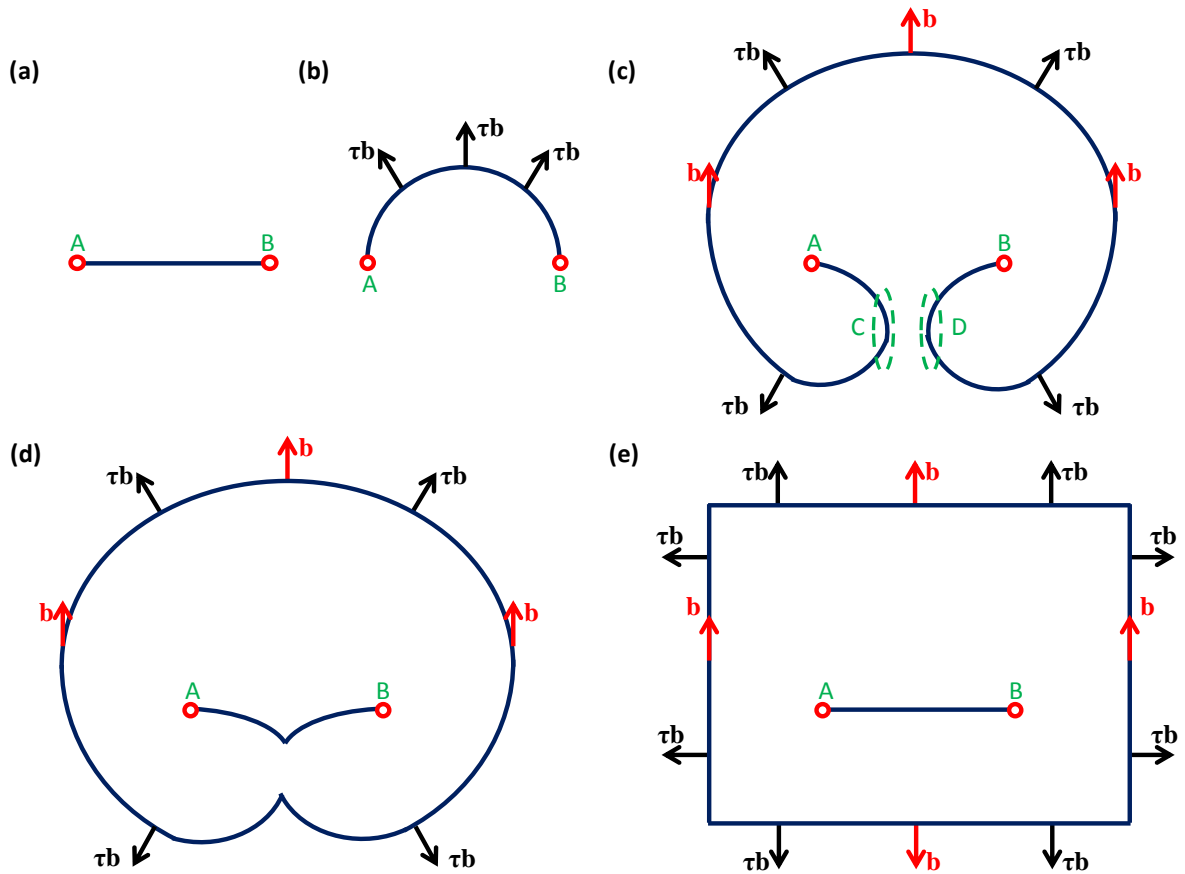Figure 2: Mechanism of dislocation pile-up formation at a high angle boundary.

Figure 3: Multiplication process via Frank-Read source: (a) initial dislocation configuration, (b) at maximum stress, (c) continuation of loop expansion under decreasing stress, (d) mutual annihilation of segments 'C' and 'D' via overlap and (e) a simple model consisting of edge and screw dislocations.
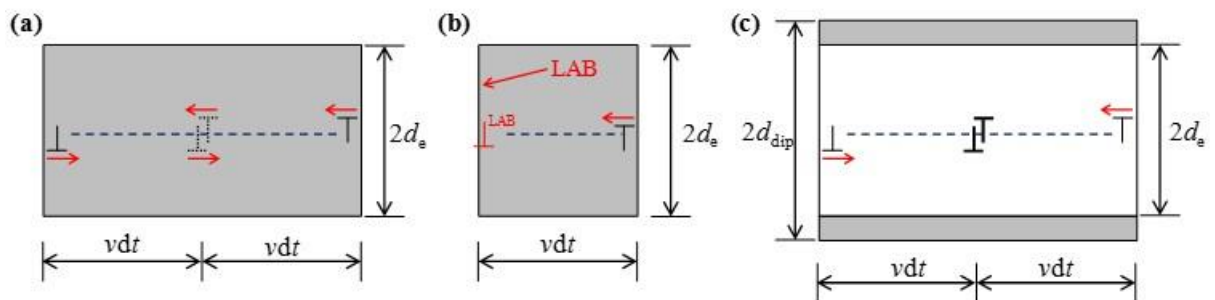


Figure 4: Schematic representation of (a) mutual dislocation annihilation, (b) LAB dislocation annihilation and (c) dipole dislocation formation.
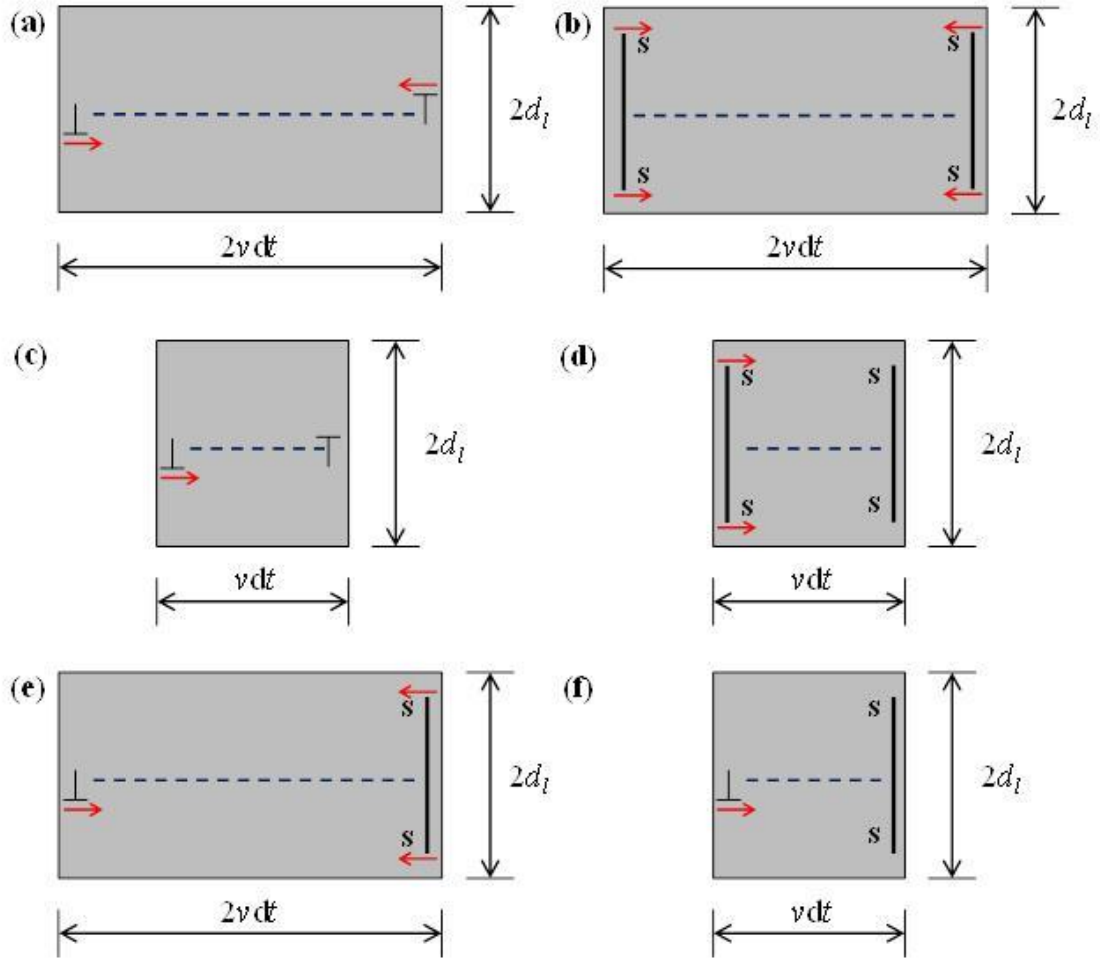
Figure 5: Formation of locked configurations for (a) edge-edge, (b) screw-screw, (c) edge-immobile edge, (d) screw-immobile screw, (e) edge-screw and (f) edge-immobile screw.
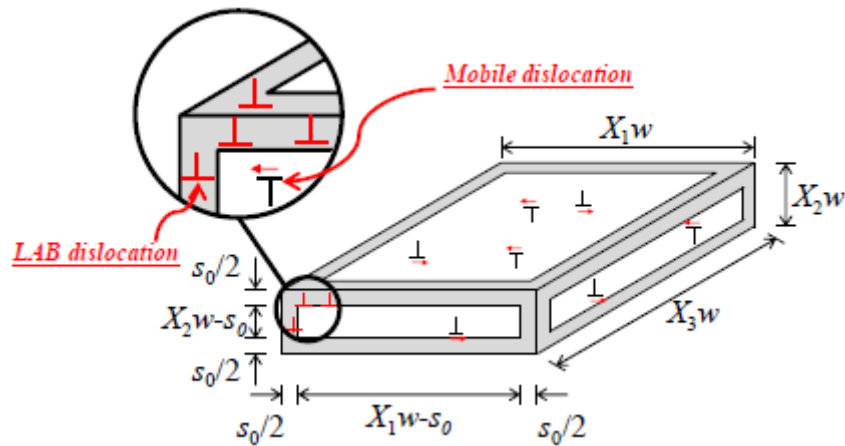


Figure 6: Representative model for the LAB microstructure. The shaded regions represent the LAB regions.
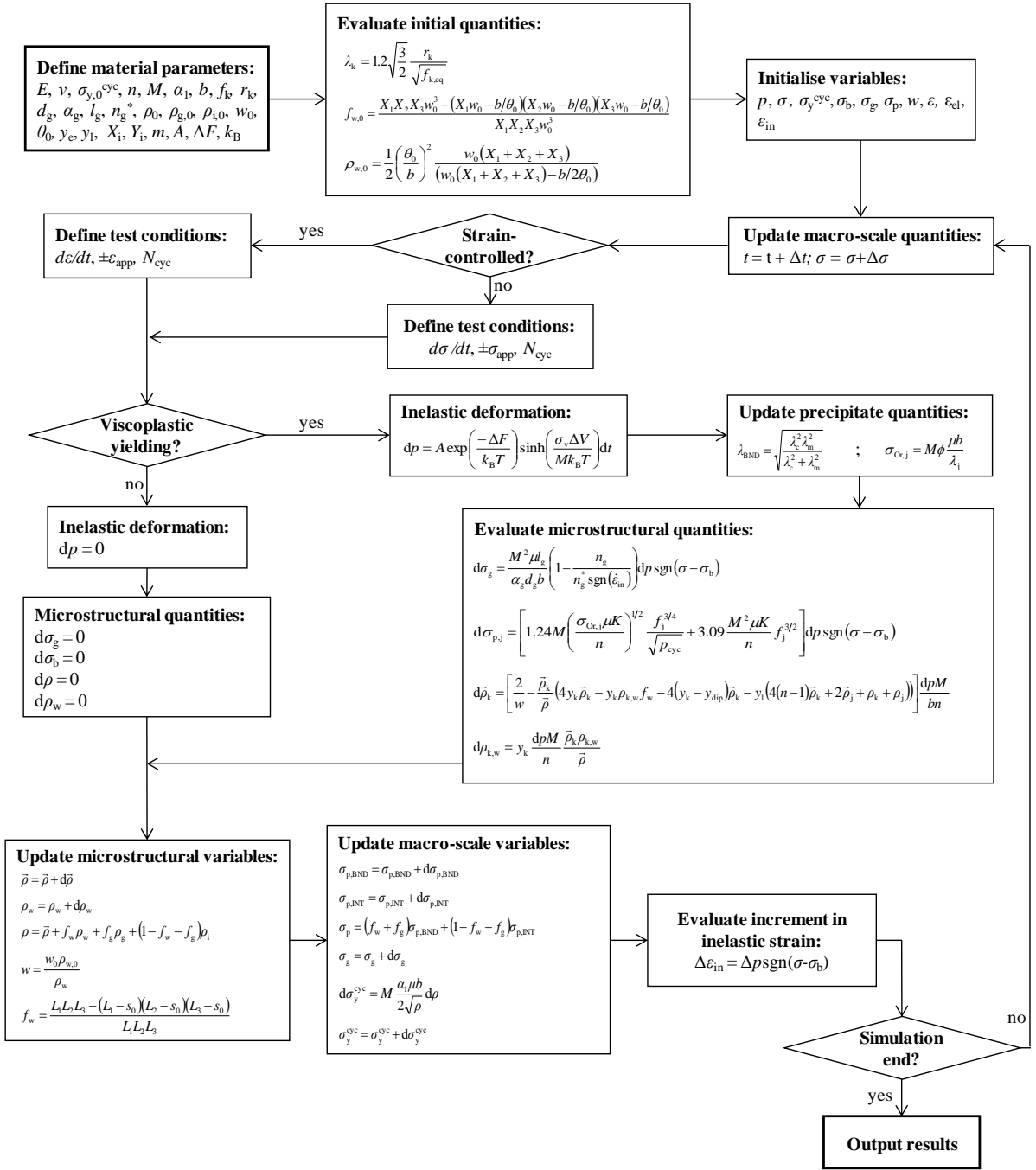
**Define material parameters:**
$E$, $v$, $\sigma_{y,0}^{cyc}$, $n$, $M$, $\alpha_1$, $b$, $f_k$, $r_k$, $d_g$, $\alpha_g$, $l_g$, $n_g^*$, $\rho_0$, $\rho_{g,0}$, $\rho_{i,0}$, $w_0$, $\theta_0$, $y_e$, $y_l$, $X_i$, $Y_i$, $m$, $A$, $\Delta F$, $k_B$

**Evaluate initial quantities:**

$$\lambda_k = 1.2\sqrt{\frac{3}{2}}\frac{r_k}{\sqrt{f_{k,eq}}}$$

$$f_{w,0} = \frac{X_1 X_2 X_3 w_0^3 - (X_1 w_0 - b/\theta_0)(X_2 w_0 - b/\theta_0)(X_3 w_0 - b/\theta_0)}{X_1 X_2 X_3 w_0^3}$$

$$\rho_{w,0} = \frac{1}{2}\left(\frac{\theta_0}{b}\right)^2 \frac{w_0(X_1 + X_2 + X_3)}{(w_0(X_1 + X_2 + X_3) - b/2\theta_0)}$$

**Initialise variables:**
$p$, $\sigma$, $\sigma_y^{cyc}$, $\sigma_b$, $\sigma_g$, $\sigma_p$, $w$, $\varepsilon$, $\varepsilon_{el}$, $\varepsilon_{in}$

**Update macro-scale quantities:**
$t = t + \Delta t$; $\sigma = \sigma + \Delta\sigma$

**Strain-controlled?** — yes →

**Define test conditions:**
$d\varepsilon/dt$, $\pm\varepsilon_{app}$, $N_{cyc}$

no →

**Define test conditions:**
$d\sigma/dt$, $\pm\sigma_{app}$, $N_{cyc}$

**Viscoplastic yielding?** — yes →

**Inelastic deformation:**
$$dp = A\exp\left(\frac{-\Delta F}{k_B T}\right)\sinh\left(\frac{\sigma_v \Delta V}{M k_B T}\right)dt$$

**Update precipitate quantities:**
$$\lambda_{BND} = \sqrt{\frac{\lambda_c^2 \lambda_m^2}{\lambda_c^2 + \lambda_m^2}} \quad ; \quad \sigma_{Or,j} = M\phi\frac{\mu b}{\lambda_j}$$

no ↓

**Inelastic deformation:**
$dp = 0$

**Evaluate microstructural quantities:**

$$d\sigma_g = \frac{M^2 \mu l_g}{\alpha_g d_g b}\left(1 - \frac{n_g}{n_g^* \operatorname{sgn}(\dot\varepsilon_{in})}\right)dp\operatorname{sgn}(\sigma - \sigma_b)$$

$$d\sigma_{p,j} = \left[1.24M\left(\frac{\sigma_{Or,j}\mu K}{n}\right)^{1/2}\frac{f_j^{3/4}}{\sqrt{p_{cyc}}} + 3.09\frac{M^2 \mu K}{n}f_j^{3/2}\right]dp\operatorname{sgn}(\sigma - \sigma_b)$$

$$d\bar\rho_k = \left[\frac{2}{w} - \frac{\bar\rho_k}{\bar\rho}\left(4y_k\bar\rho_k - y_k\rho_{k,w}f_w - 4(y_k - y_{dip})\bar\rho_k - y_l(4(n-1)\bar\rho_k + 2\bar\rho_j + \rho_k + \rho_j)\right)\right]\frac{dpM}{bn}$$

$$d\rho_{k,w} = y_k\frac{dpM}{n}\frac{\bar\rho_k\rho_{k,w}}{\bar\rho}$$

**Microstructural quantities:**
$d\sigma_g = 0$
$d\sigma_b = 0$
$d\rho = 0$
$d\rho_w = 0$

**Update microstructural variables:**
$\bar\rho = \bar\rho + d\bar\rho$
$\rho_w = \rho_w + d\rho_w$
$\rho = \bar\rho + f_w\rho_w + f_g\rho_g + (1 - f_w - f_g)\rho_i$
$w = \dfrac{w_0\rho_{w,0}}{\rho_w}$
$f_w = \dfrac{L_1 L_2 L_3 - (L_1 - s_0)(L_2 - s_0)(L_3 - s_0)}{L_1 L_2 L_3}$

**Update macro-scale variables:**
$\sigma_{p,BND} = \sigma_{p,BND} + d\sigma_{p,BND}$
$\sigma_{p,INT} = \sigma_{p,INT} + d\sigma_{p,INT}$
$\sigma_p = (f_w + f_g)\sigma_{p,BND} + (1 - f_w - f_g)\sigma_{p,INT}$
$\sigma_g = \sigma_g + d\sigma_g$
$d\sigma_y^{cyc} = M\dfrac{\alpha_1\mu b}{2\sqrt\rho}d\rho$
$\sigma_y^{cyc} = \sigma_y^{cyc} + d\sigma_y^{cyc}$

**Evaluate increment in inelastic strain:**
$\Delta\varepsilon_{in} = \Delta p\operatorname{sgn}(\sigma - \sigma_b)$

**Simulation end?** — no / yes →

**Output results**

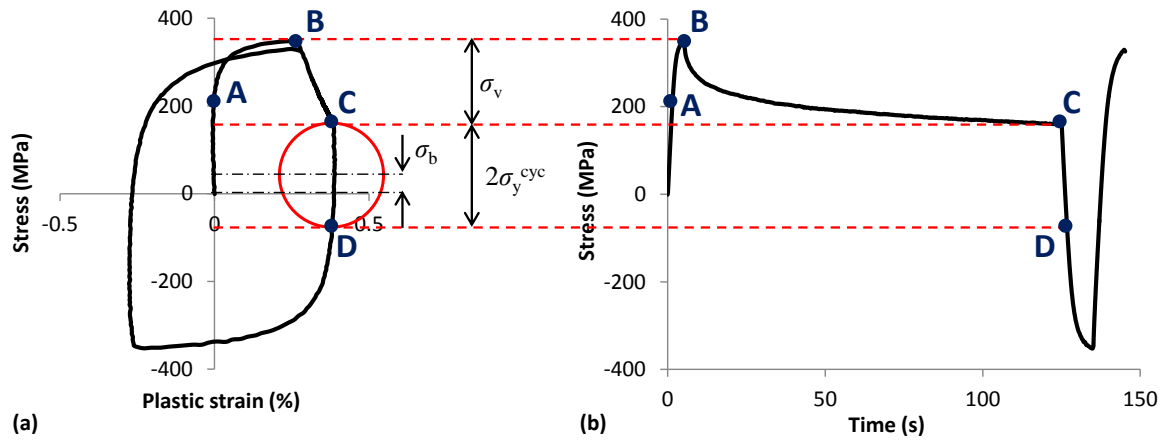Figure 7: Flowchart of the main processes in the uniaxial model.

34

Figure 8: Identification of the components of stress from the initial cycle in a dwell test at 600 °C using Cottrell's method.
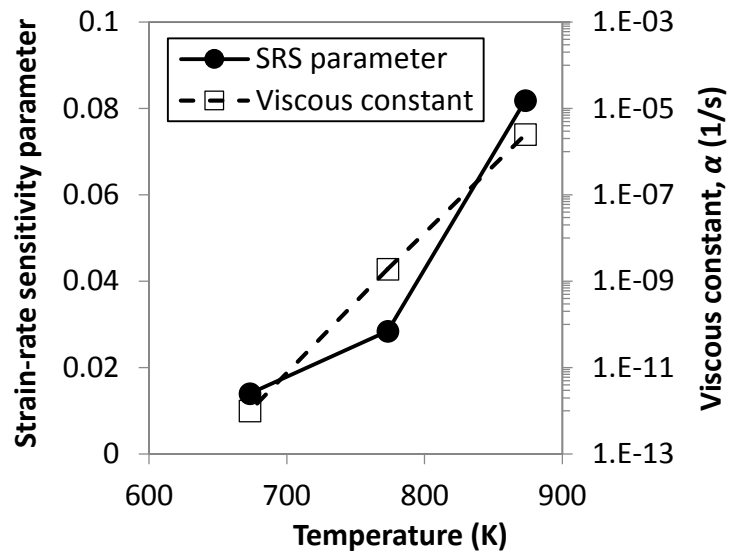


Figure 9: Identified strain-rate sensitivity (SRS) parameter and viscous constant as a function of temperature for P91 steel.
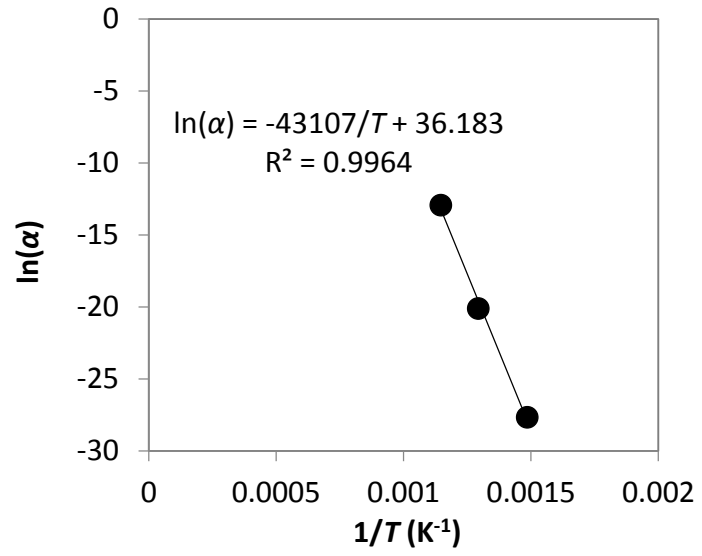
Figure 10: Identification of Helmholtz free energy and the pre-exponential constant for P91 steel.
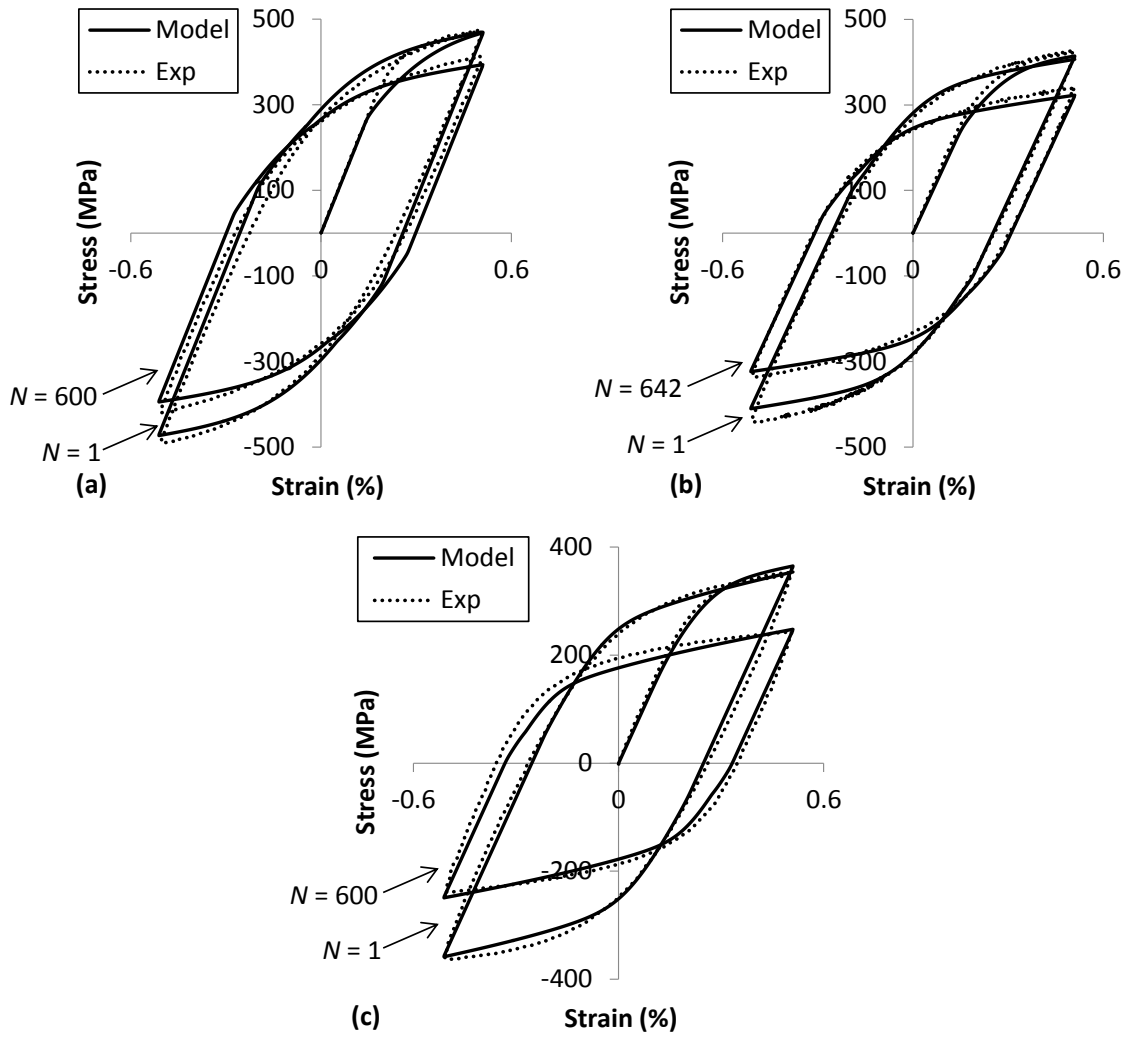
Figure 11: Comparison of the experimentally-measured and predicted evolutions of stress-strain response for temperatures of (a) 400 °C, (b) 500 °C and (c) 600 °C under calibration conditions of an applied strain-range of ±0.5 % and strain-rate of 0.01 %/s.
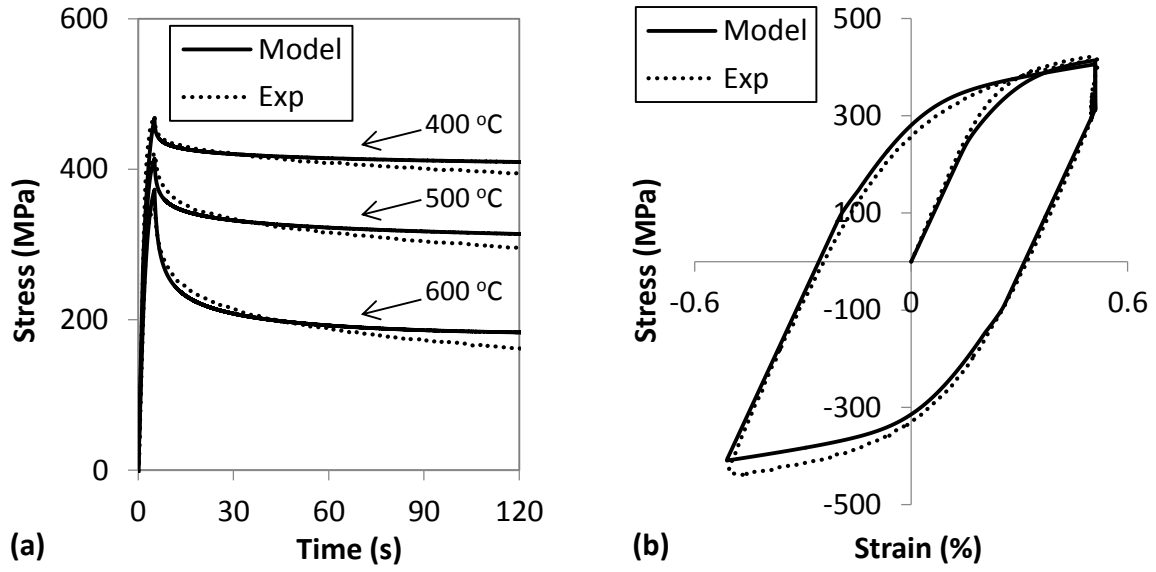
Figure 12: Comparison of the measured and predicted (a) stress relaxation response as a function of time at temperatures of 400 °C, 500 °C and 600 °C and (b) stress-strain response at 500 °C. The applied strain is ±0.5 %.
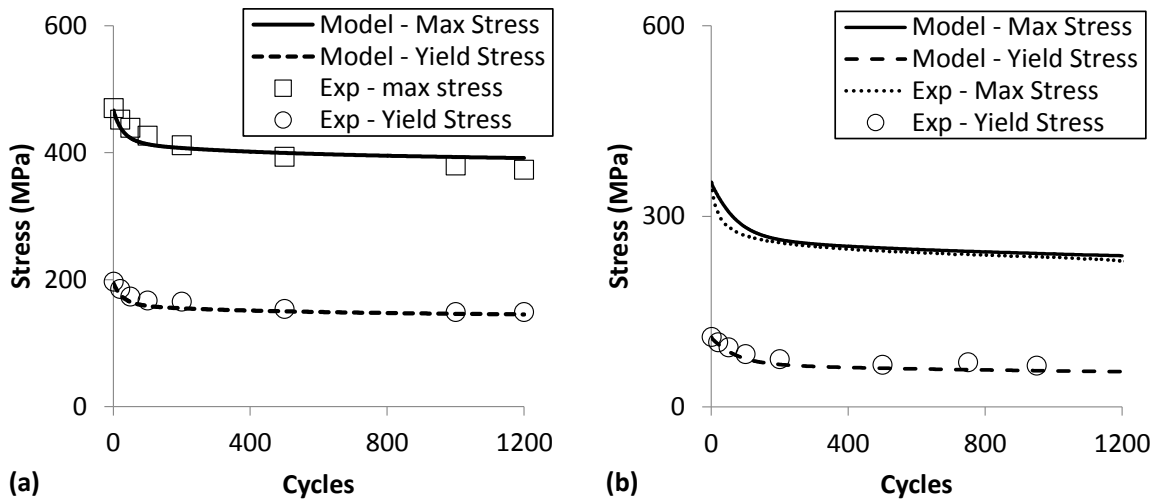


Figure 13: Comparison of experimentally observed and model predicted maximum and cyclic yield stress evolution as a function of cycles in P91 steel at temperatures of (a) 400 °C and (b) 600 °C, applied strain-range of ±0.5 % and strain-rate of 0.1 %/s.
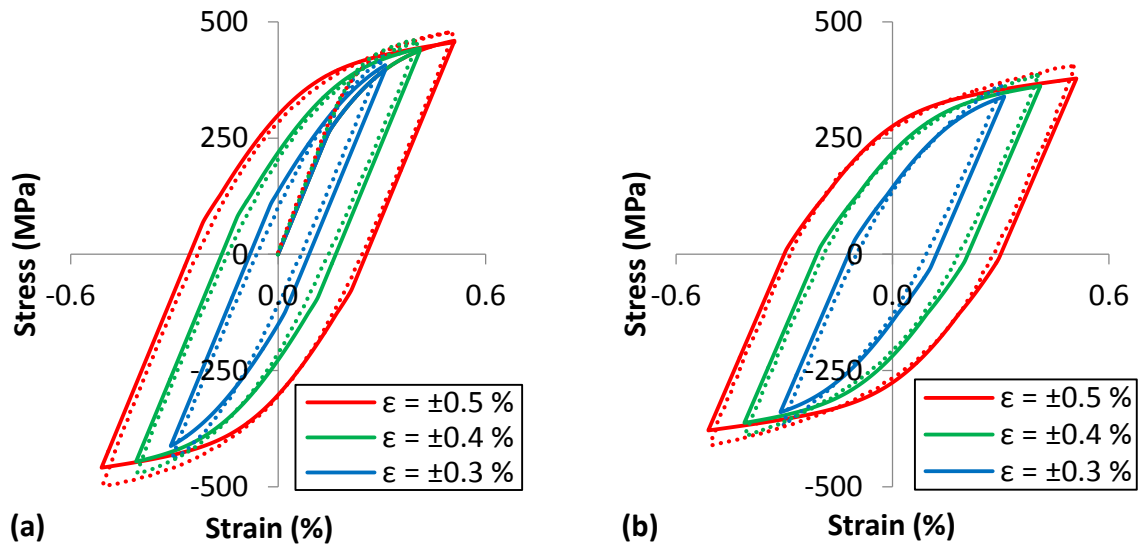
Figure 14: Comparison of the measured and predicted stress-strain response for an applied strain-rate of 0.033 %/s for (a) the initial and (b) half life cycles at 400 °C across strain-ranges of ±0.3 %, ±0.4 % and ±0.5 %. The dotted lines represent experimental data and the solid lines are the model predictions.
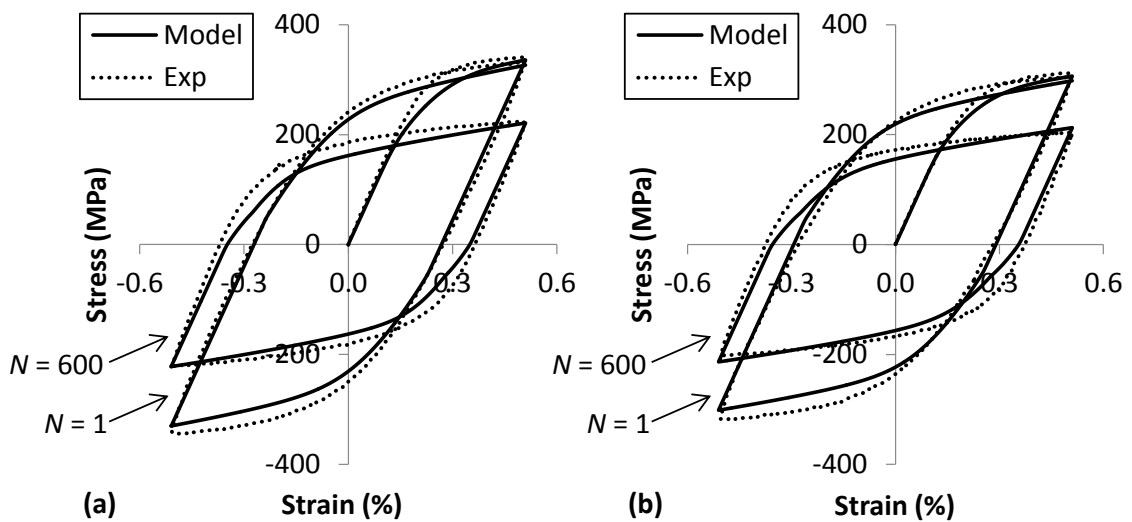


Figure 15: Comparison of the measured and predicted stress-strain response at 600 °C for applied strain-rates of (a) 0.033 %/s and (b) 0.025 %/s.
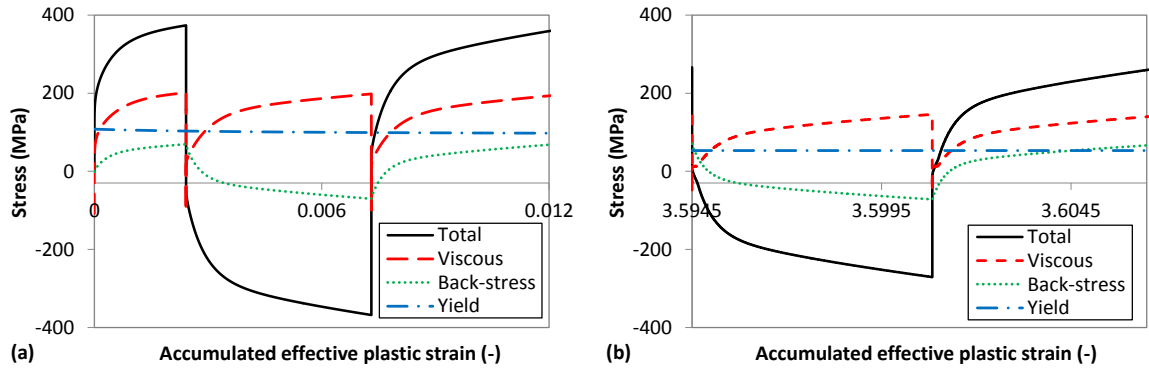
Figure 16: Simulated components of stress as a function of accumulated effective plastic strain for the (a) initial cycle and (b) 300th cycle at 600 °C, applied strain-range of ±0.5 % and a strain-rate of 0.1 %/s.
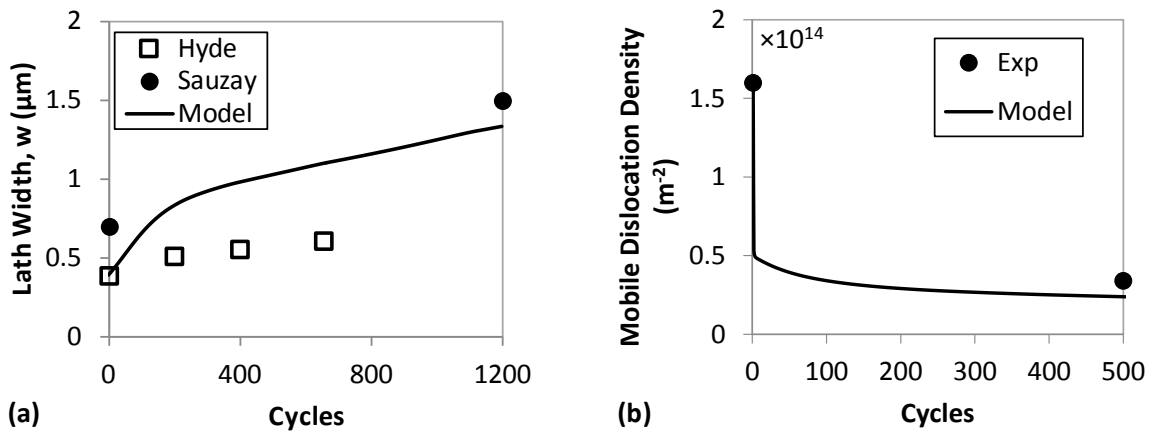


Figure 17: Comparison of predicted microstructural evolution with measured data at 600 °C for (a) martensitic lath width (test data of [16,86]) and (b) mobile dislocation density (data of [16]). The applied strain-range is ±0.5 % and a strain-rate of 0.1 %/s. Note that the experimental testing of Sauzay *et al.* [16] was carried out at 550 °C.
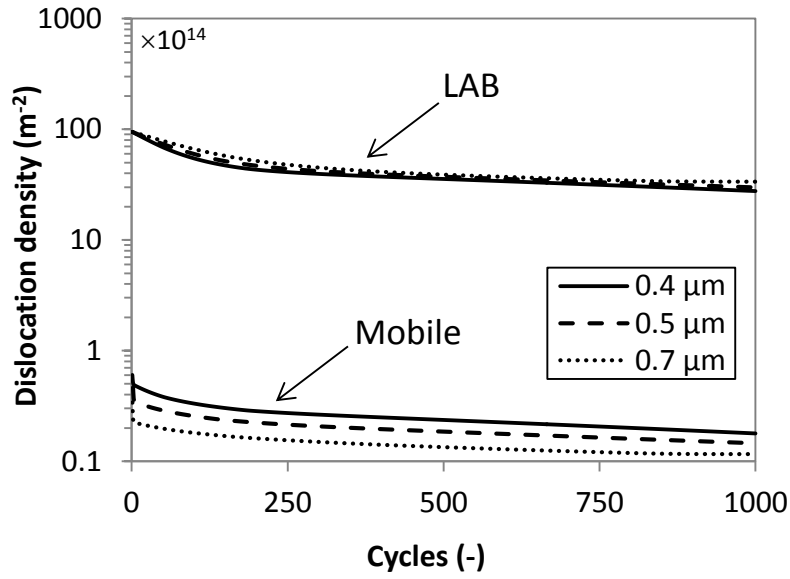
Figure 18: Predicted cyclic evolution of mobile dislocation density (mobile) and low-angle boundary dislocation density (LAB) at 600 °C in P91 steel for different initial lath widths. The applied strain-range is ±0.5 % and a strain-rate of 0.025 %/s.
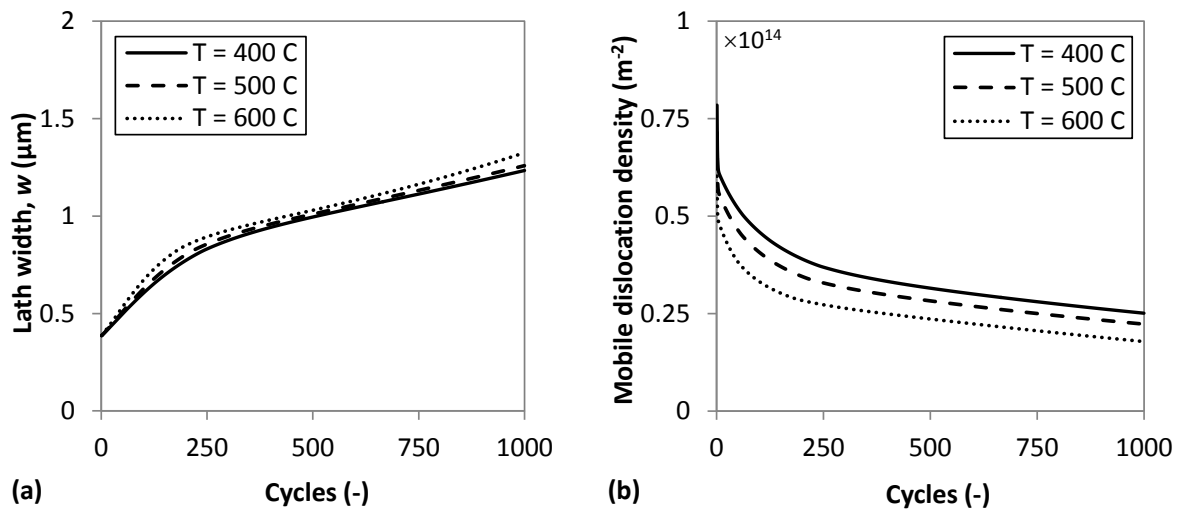


Figure 19: Predicted effect of temperature on (a) martensitic lath width and (b) mobile dislocation density with cyclic evolution. The applied strain-range is ±0.5 % and a strain-rate of 0.033 %/s.
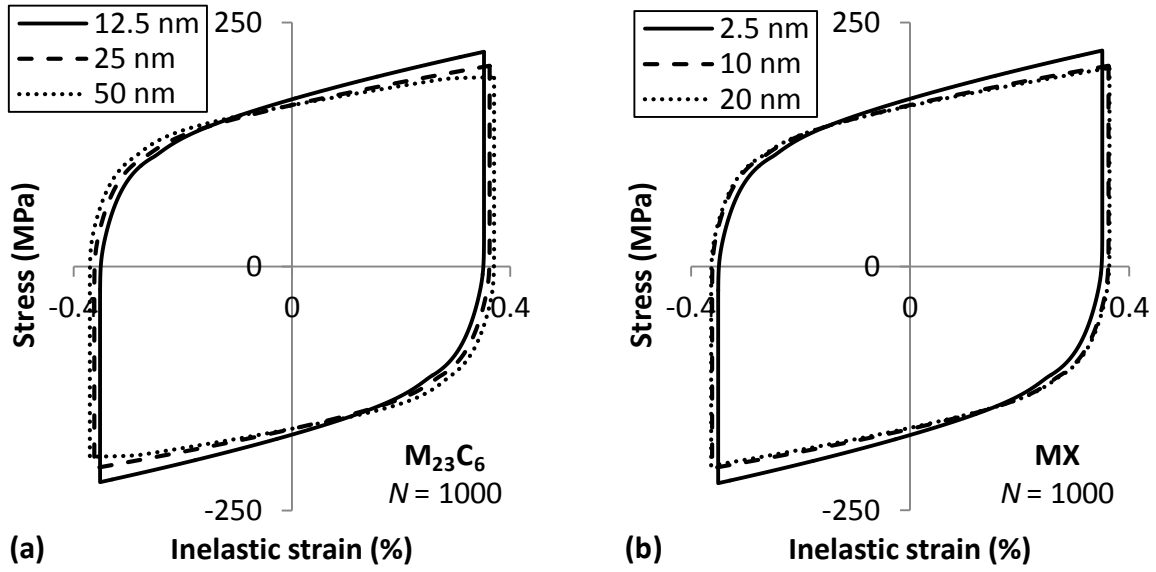
Figure 20: Predicted effect of varying the mean square radius, $r_k$, of (a) $M_{23}C_6$ carbides and (b) MX carbonitrides for the 1000th cycle in P91 steel at a temperature of 600 °C. The strain-rate is 0.025 %/s and the strain-range is ±0.5 %.
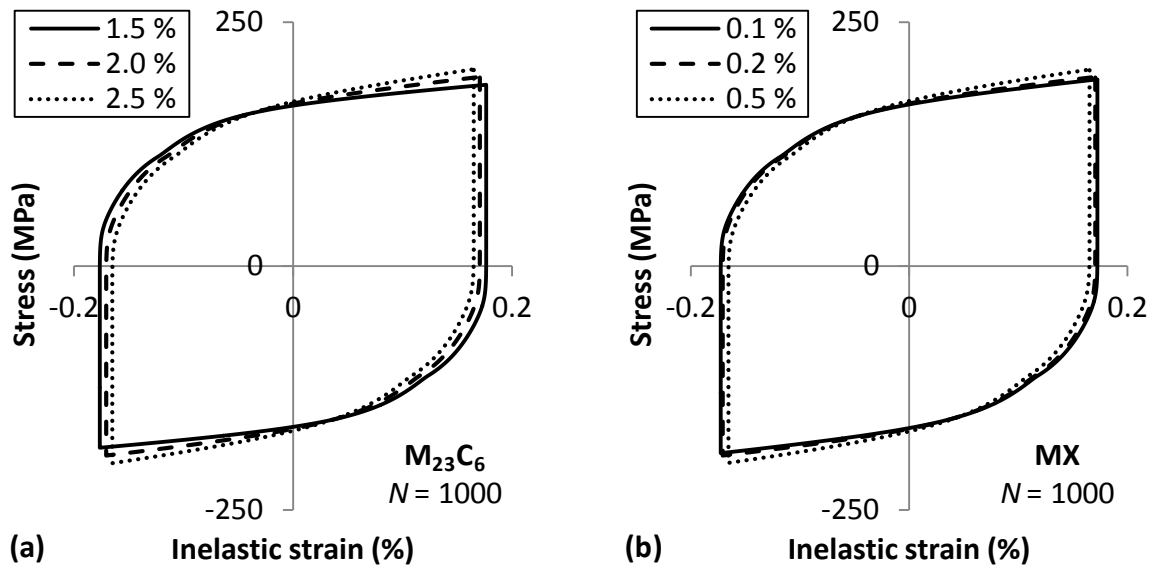


Figure 21: Predicted effect of volume fraction, $f_k$, of (a) $M_{23}C_6$ carbides and (b) MX carbonitrides for the 1000th cycle in P91 steel at a temperature of 600 °C. The strain-rate is 0.025 %/s and the strain-range is ±0.3 %.
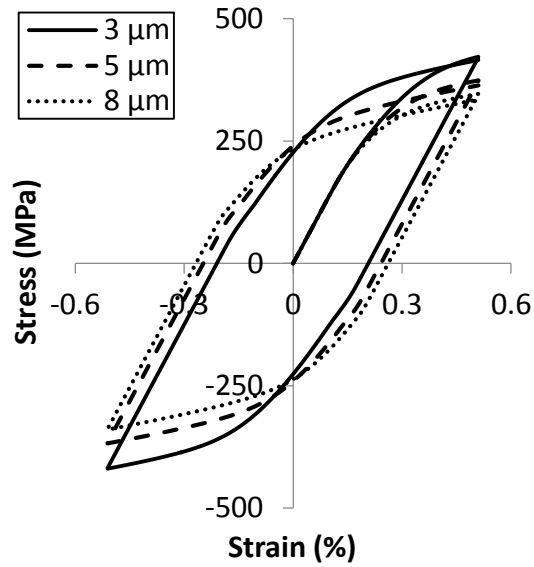
Figure 22: Predicted effect of varying the block width in P91 steel for the initial cycle at 600 °C. The strain-rate is 0.1 %/s and the strain-range is ±0.5 %.
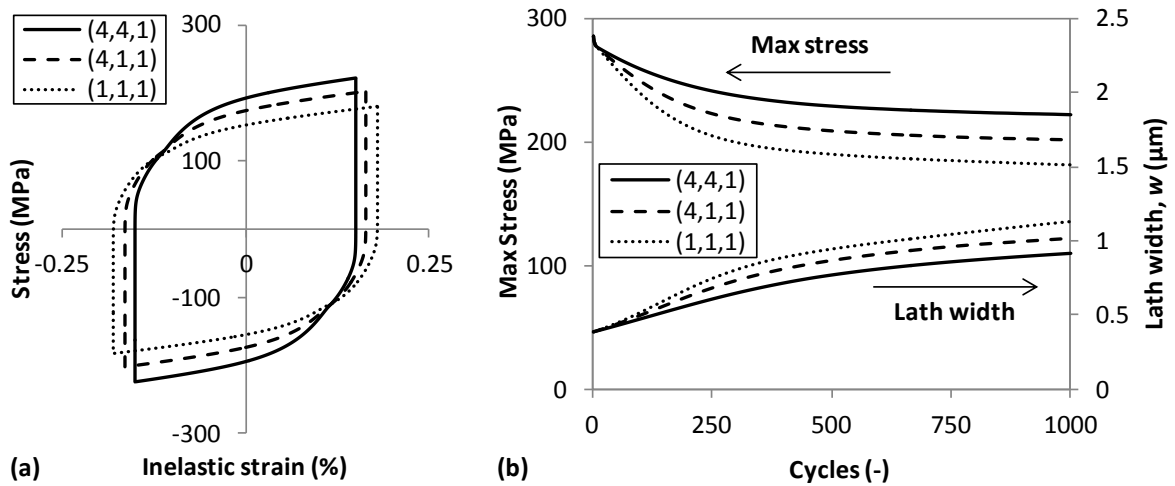


Figure 23: Predicted effect of lath shape at 600 °C on (a) stress-inelastic strain response for the 1000<sup>th</sup> cycle and (b) maximum stress and lath width evolution as a function of cycles for an applied strain-range of ±0.3 % and a strain-rate of 0.033 %/s.
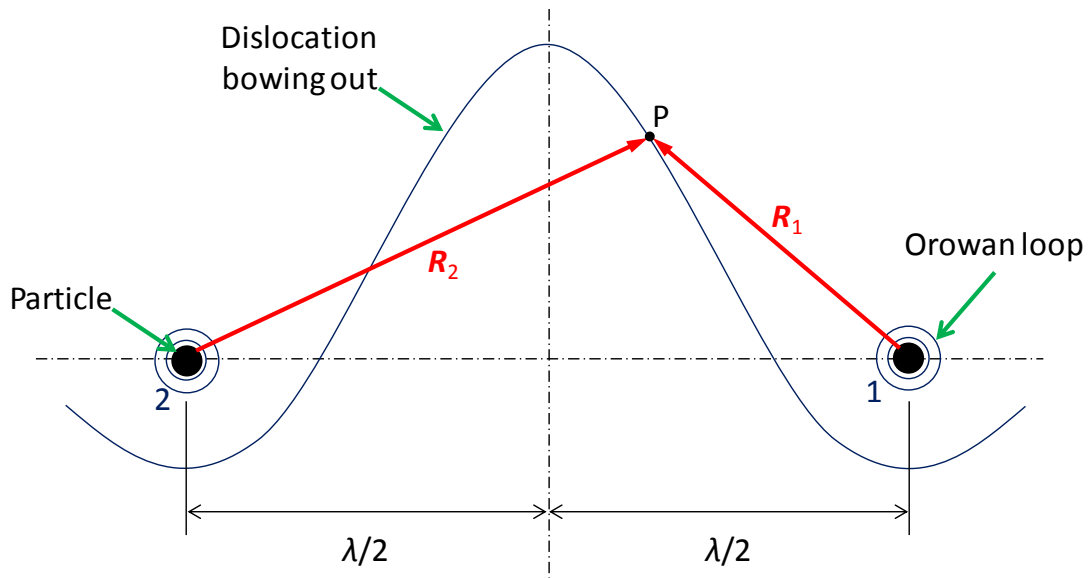
Figure 24: Schematic representation of a dislocation pinned at two particles.

## References

1. Maruyama, K., Sawada, K., Koite, J. Strengthening mechanisms of creep resistant tempered martensitic steel. ISIJ International, **41** (2001), pp. 641-653.

2. Abe, F. Precipitate design for creep strengthening of 9% Cr tempered martensitic steel for ultra-supercritical power plants. Science and Technology of Advanced Materials, **9** (2008), pp. 013002 (1-15).

3. Chauhan, A., Litvinov, D., de Carlan, Y., Aktaa, J. Study of the deformation and damage mechanisms of a 9Cr-ODS steel: Microstructure evolution and fracture characteristics. *Materials Science and Engineering A*, **658** (2016), pp. 123-134.

4. Ennis, P.J., Czyrska-Filemonowicz, A. Recent advances in creep resistant materials for power plant applications. Power Plant Operation, Maintenance and Material Issues (OMMI), **1** (2002), pp. 1-28.

5. Hu, X., Huang, L., Yan, W., Wang, W., Sha, W., Shan, Y., Yang, K. Low cycle fatigue properties of CLAM steel at 823 K. Materials Science and Engineering A, **613** (2014), pp. 404-413.

6. Panait, C.G., Zielińska-Lipiec, A., Koziel, T., Czyrska-Filemonowicz, A., Gourgues-Lorenzon, A.-F., Bendick, W. Evolution of dislocation density, size of subgrains and MX-type precipitates in a P91 steel during creep and thermal aging at 600 °C for more than 100,000 h. Materials Science and Engineering A, **527** (2010), pp. 4062-4069.

7. Saad, A.A., Hyde, C.J., Sun, W., Hyde, T.H. Thermal-mechanical fatigue simulation of a P91 steel in a temperature range of 400-600 °C. Materials at High Temperature, **28** (2011), pp. 212-218.

8. Saad, A.A., Sun, W., Hyde, T.H., Tanner, D.W.J. Cyclic softening behaviour of a P91 steel under low cycle fatigue at high temperature. Procedia Engineering, **10** (2011), pp. 1103-1108.

9. Nagesha, A., Valsan, M., Kannan, R., Bhanu Sankara Rao, K., Mannan, S.L. Influence of temperature on the low cycle fatigue behaviour of a modified 9Cr-1Mo ferritic steel. International Journal of Fatigue, **24** (2002), pp. 1285-1293.

10. Fournier, B., Sauzay, M., Caës, C., Noblecourt, M., Mottot, M., Allais, L., Tournie, I., Pineau, A. Creep-fatigue interactions in a 9 Pct Cr-1 Pct Mo martensitic steel: Part I. Mechanical test results. Metallurgical and Materials Transactions A, (2009) **40** 321-329.

11. Giroux, P.-F. Experimental study and simulation of cyclic softening of tempered martensite ferritic steels. Ph.D. thesis, l'École Nationale Supérieure des Mines de Paris, 2011.

12. Mannan, S.L., Valsan, M. High-temperature low cycle fatigue, creep-fatigue and thermomechanical fatigue of steels and their welds. International Journal of Mechanical Sciences, **48** (2006), pp. 160-175.

13. Farragher, T.P. Thermomechanical analysis of P91 power plant components. Ph.D. Thesis, National University of Ireland, Galway (2014).

14. Nabarro, F. Creep at very low rates. Metallurgical and Materials Transactions A, **33** (2002), pp. 213-218.

15. Sauzay, M., Brillet, H., Monnet, I, Mottot, M., Barcelo, F., Fournier, B., Pineau, A. Cyclically induced softening due to low-angle boundary annihilation in a martensitic steel. Materials Science and Engineering A, **400-401** (2005), pp. 241-244.

16. Sauzay, M., Fournier, B., Mottot, M., Pineau, A., Monnet, I. Cyclic softening of martensitic steels at high temperature – Experiments and physically based modelling. Materials Science and Engineering A, **483-484** (2008), pp. 410-414.

17. Barrett, R.A., Farragher, T.P., Hyde, C.J., O'Dowd, N.P., O'Donoghue, P.E., Leen, S.B. A unified viscoplastic model for high temperature low cycle fatigue of service-aged P91 steel. Transactions of the ASME Journal of Pressure Vessel Technology, **136** (2014), pp. 021402.

18. Barrett R.A. Experimental characterisation and computational constitutive modelling of high temperature degradation in 9Cr steels including microstructural effects. Ph.D. Thesis, National University of Ireland, Galway (2016)

19. Barrett, R.A., O'Hara, E.M., O'Donoghue, P.E., Leen, S.B. High-temperature low-cycle fatigue behaviour of MarBN at 600 °C. Transactions of the ASME Journal of Pressure Vessel Technology, **138** (2016), pp. 041401.

20. Hyde, C.J., Sun, W., Hyde, T.H., Saad, A.A. Thermo-mechanical fatigue testing and simulation using a viscoplasticity model for P91 steel. Computational Materials Science, **56** (2012), pp. 29-33.

21. Hu, X., Li, L., Wu., X., Zhang, M. Coarsening behaviour of $M_{23}C_6$ carbides after aging or thermal fatigue in AISI H13 steel with niobium. Int. J. Fatigue, **28** (2006) pp. 175-182.

22. Hu, X., Huang, L., Yan, W., Wang, W., Sha, W., Shan, Y., Yang, K. Low cycle fatigue properties of CLAM steel at 823 K. Materials Science and Engineering A, **613** (2014), pp. 404-413.

23. Giordana, M.F., Giroux, P.-F., Alvarez-Armas, I., Sauzay, M., Armas, A., Kruml, T. Microstructure evolution during cyclic tests on EUROFER 97 at room temperature. TEM observation and modelling. Materials Science and Engineering A, **550** (2012), pp. 103-111.

24. Marmy, P., Kruml, T. Low cycle fatigue of Eurofer 97. J. of Nuclear Materials, **377** (2008) pp. 52-58.

25. Chaboche, J.L., Rousselier, G. On the plastic and viscoplastic constitutive equations – part I: rules developed with internal variable concept. Transactions of the ASME Journal of Pressure Vessel Technology, **105** (1983), pp. 153-158.

26. Chaboche, J.L., Rousselier, G. On the plastic and viscoplastic constitutive equations – part II: Application of internal variable concepts to the 316 stainless steel. Transactions of the ASME Journal of Pressure Vessel Technology, **105** (1983), pp. 159-164.

27. Farragher, T.P., Scully, S., O'Dowd, N.P., Leen, S.B. Thermomechanical analysis of a pressurised pipe under plant conditions. Transactions of the ASME Journal of Pressure Vessel Technology, **135** (2013), pp. 011204.

28. Farragher, T.P., Scully, S., O'Dowd, N.P., Hyde, C.J., Leen, S.B. High temperature, low cycle fatigue characterisation of P91 weld and heat affected zone material. Transactions of the ASME Journal of Pressure Vessel Technology, **136** (2014), pp. 021403.

29. Miller, A.K. The MATMOD equations. In: Miller, A.K. (Ed.). Unified constitutive equations for creep and plasticity. London: Elsevier Applied Science; 1987, pp. 139-220.

30. Barrett R.A., O'Donoghue, P.E., Leen, S.B. An improved unified viscoplastic constitutive model for strain-rate sensitivity in high temperature fatigue. Int. J. Fatigue, **48** (2013) pp. 192-204.

31. Dunne, F.P.E., Rugg, D., Walker, A. Lengthscale-dependent, elastically anisotropic, physically-based hcp crystal plasticity: Application to cold-dwell fatigue in Ti alloys. *International Journal of Plasticity*, **23** (2007) 1061-1083.

32. Sellars, C.M., Tegart, W.J. Mem. Sci. Rev. Met. **63** (1966) 731

33. Wong, W.A., Jonas, J.J. Trans. AIME, **242** (1968) 2271.

34. Dyson, B.F., McLean, M. In: Strang, A., Cawley, J., Greenwood, G.W. (Eds.): Microstructural stability of creep resistant alloys for high temperature plant applications. Institute of Materials: London (1998), pp. 371-392.

35. Chateau, E., Rémy, L. Oxidation-assisted creep damage in a wrought nickel based superalloy: experiments and modelling. *Materials Science and Engineering A*, **527** (2010) 1655-1664.

36. Szmytka, F., Rémy, L., Maitournam, H., Köster, A. New flo rules in elasto-viscoplastic constitutive model for spheroidal graphite cast iron. *International Journal of Plasticity*, **26** (2010) 905-924.

37. Rémy, L., Szmytka, F., Bucher, L. Constitutive models for bcc engineering iron alloys exposed to thermal-mechanical fatigue. *International Journal of Fatigue*, **53** (2013) 2-14.

38. Li, D.-F., Barrett, R.A., O'Donoghue, P.E., Hyde, C.J., O'Dowd, N.P., Leen, S.B. Micromechanical finite element modelling of thermo-mechanical fatigue for P91 steels. Int. J. Fatigue, **87** (2016) pp. 192-202.

39. Li., D.-F., Golden, B.J., O'Dowd, N.P. Multi-scale modelling of mechanical response in a martensitic steel: A micromechanical and length-scale dependent framework for precipitate hardening. Acta Materialia, **80** (2014) pp. 445-456.

40. Spigarelli, S. Microstructure-based assessment of creep rupture strength in 9Cr steels. Int. J. Pressure Vessel and Piping **101** (2013) pp. 64-71.

41. Magnusson, H., Sandström, R. Creep strain modelling of 9 to 12 Pct Cr steels based on microstructure evolution. Metallurgical and materials transactions A, **38** (2007), pp. 2033-2039.

42. Oruganti, R., Karadge, M., Swaminathan, S. Damage mechanics-based creep model for 9-10%Cr ferritic steels. Acta Materialia, **59** (2011), pp. 2145-2155.

43. Fournier, B., Sauzay, M., Pineau, A. Micromechanical model of the high temperature cyclic behaviour of 9-12%Cr martensitic steels. *International Journal of Plasticity*, **27** (2011) 1803-1816.

44. Barrett, R.A., O'Donoghue, P.E., Leen, S.B. A dislocation-based model for high temperature cyclic viscoplasticity of 9-12Cr steels. Computational Materials Science, **92** (2014) pp. 286-297.

45. Gibbs, G.B. Thermodynamic analysis of dislocation glide controlled by dispersed local obstacles. *Materials Science and Engineering A*, **4** (1969) 313-328.

46. Orowan, E. Problems of plastic gliding. Proceedings of the Physical Society, **52** (1940), pp. 8-22.

47. Taylor, G.I. Plastic strain in Metals. Journal of the Institute of Metals, **62** (1938), pp. 307-324.

48. Zener, C. Theory of diffusion. In: Shockley, W., Hollomon, J.H., Maurer, R. (Eds.). Imperfections in Nearly Perfect Crystals. New York: John Wiley and Sons Inc. (1952) pp. 289-314.

49. Basirat, M., Shrestha, T., Potirniche, G.P., Charit, I., Rink, K. A study of the creep behaviour of modified 9Cr-1Mo steel using continuum-damage modeling. *International Journal of Plasticity*, **37** (2012) 95-107.

50. Dyson, B. Use of CDM in materials modelling and component creep life prediction. *Transactions of the ASME Journal of Pressure Vessel Technology*, **122** (2000) 281-296.

51. Haseeb, A.S.M.A. Modeling of the effects of athermal flow strength and activation energy for dislocation glide on the nanoindentation creep of nickel thin film at room temperature. *Computational Materials Science*, **37** (2006) 278-283.

52. Sweeney, C.A., Vorster, W., Leen, S.B., Sakurada, E., McHugh, P.E., Dunne, F.P.E. The role of elastic anisotropy, length scale and crystallographic slip in fatigue crack nucleation. *Journal of the Mechanics and Physics of Solids*, **61** (2013) 1224-1240.

53. Reed-Hill, R.E., Abbaschian, R. Physical Metallurgy Principles. 3$^{rd}$ edition. PWS Publishing Company: Boston (1992).

54. Keller, C., Margulies, M.M., Hadjem-Hamouche, Z., Guillot, I. Influence of the temperature on the tensile behaviour of a modified 9Cr-1Mo T91 martensitic steel. *Materials Science and Engineering A*, **527** (2010) 6758-6764.

55. Estrin, Y., Braasch, H., Brechet, Y. A dislocation density based constitutive model for cyclic deformation. *Journal of Engineering Materials and Technology*, **118** (1996) 441-447.

56. Estrin, Y. Dislocation theory based constitutive modelling: foundations and applications. *Journal of Materials Processing Technology*, **80-81** (1998) 33-39.

57. Kocks, U.F., Argon, A.S., Ashby, M.F. Thermodynamics and Kinetics of Slip. Pergamon Press: Oxford (1975).

58. Shrestha, T., Basirat, M., Charit, I., Potirniche, G.P., Rink, K.K., Sahaym, U. Creep deformation mechanisms in modified 9Cr-1Mo steel. *Journal of Nuclear Materials*, **423** (2012) 110-119.

59. Ye, Z., Wang, P., Li, D., Zhang, Y., Li, Y. Effect of carbon and niobium on the microstructure and impact toughness of a high silicon 12% Cr ferritic/martensitic heat resistant steel. *Materials Science and Engineering A*, **616** (2014) 12-19.

60. Estrin, Y., Tóth, L.S., Molinari, A., Bréchet, Y. A dislocation-based model for all hardening stages in large strain deformation. *Acta Materialia*, **46** (1998) 5509-5522.

61. Hart, E.W. Theory of dispersion hardening in metals. *Acta Metallurgica*, **20** (1972) 275-289.

62. Roters, F., Raabe, D., Gottstein, G. Work hardening in heterogeneous alloys – A microstructural approach based on three internal state variables. Acta Materialia, **48** (2000), pp. 4181-4189.

63. Kocks, U.F. On the spacing of dispersed obstacles. *Acta Metallurgica, 14 (1966) 1629-1631.*

64. Zhang, Z.F., Wang, Z.G. Comparison of fatigue cracking possibility along large- and low-angle grain boundaries. Materials Science and Engineering A, **284** (2000), pp. 285-291.

65. Ashby, M.F., Jones, D.R.H. Engineering Materials 1: An Introduction to Properties, Applications and Design. Elsevier Ltd.: Oxford (2012).

66. Sinclair, C.W., Poole, W.J., Bréchet, Y. A model for the grain size dependent work hardening of copper. Scripta Materialia, **55** (2006), pp. 739-742.

67. Bardel, D., Perez, M., Nelias, D., Dancette, S., Chaudet, P., Massardier, V. Cyclic behaviour of a 6061 aluminium alloy: Coupling precipitation and elastoplastic modelling. Acta Materialia, **83** (2015), pp. 256-268.

68. Li, J.C.M. Some elastic properties of an edge dislocation wall. Acta Materialia, **8** (1960), pp. 563-574.

69. Li, J.C.M. Petch relation and grain boundary sources. Transactions of the Metallurgical Society of AIME, **227** (1963), pp. 239-247.

70. Frank, F.C., Read, W.T. Multiplication processes for slow moving dislocations. Physical Review, **79** (1950), pp. 722-723.

71. Plumtree, A., Abdel-Raouf, H.A. Relationship between cyclic stress-strain response and substructure. In: Rie, K.T., Portella, P.D. (Eds.). Low cycle fatigue and elasto-plastic behaviour of materials. Elsevier Science Ltd.: London (1998), pp. 279-284.

72. Hosseini, E., Kazeminezhad, M. A microstructural model based on dislocation generation and consumption mechanisms through severe plastic deformation. Computational Materials Science, **50** (2011), pp. 1123-1135.

73. Essmann, U., Mughrabi, H. Annihilation of dislocations during tensile and cyclic deformation and limits of dislocation densities. Philosophical Magazine A, **40** (1979), pp. 731-756.

74. Ma, A., Roters, F. A constitutive model for fcc single crystals based on dislocation densities and its application to uniaxial compression of aluminium single crystals. Acta Materialia, **52** (2004), pp. 3603-3612.

75. Zaafarani, N., Raabe, D., Roters, F., Zaefferer, S. On the origin of deformation-induced rotation patterns below nanoindents. Acta Materialia, **56** (2008), pp. 31-42.

76. Sonderegger, B., Mitsche, S., Cerjak, H. Martensite laths in creep resistant martensitic 9-12% Cr steels – Calculation and measurement of misorientations. Materials Characterization, **58** (2007) pp. 874-882.

77. Li, Q. Modeling the microstructure-mechanical property relationship for a 12Cr-2W-V-Mo-Ni power plant steel. *Materials Science and Engineering A*, **361** (2003), pp. 385-391.

78. Maropoulos, S., Ridley, N. The dependence of mechanical properties on structure in low alloy steel forgings. *Journal of Material Sciences*, **40** (2005), pp. 4753-4759.

79. Dieter, G.E. Mechanical Metallurgy. McGraw-Hill: New York (1986).

80. Read, W.T., Shockley, W. Dislocation models of crystal grain boundaries. Physical Review, **73** (1950), pp. 275-289.

81. Ricoult, D.L., Kohlstedt, D.L. Structural width of low-angle grain boundaries in Olivine. Physics and Chemistry of Minerals, **9** (1983) pp. 133-138.

82. Cottrell, A.H. Dislocations and Plastic Flow in Crystals. Oxford University Press: Oxford (1953).

83. Wei, Q., Cheng, S., Ramesh, K.T., Ma, E. Effect of nanocrystalline and ultrafine grain sizes n the strain rate sensitivity and activation volume: fcc versus bcc metals. *Materials Science and Engineering A*, **381** (2004) 71-79.

84. Siska, F., Stratil, L., Smid, M., Luptakova, N., Zalezak, T., Bartkova, D. Deformation and fracture behaviour of the P91 martensitic steel at high temperatures. *Materials Science and Engineering A*, **672** (2016) 1-6.

85. Ijiri, Y., Oono, N., Ukai, S., Ohtsuka, S., Kaito, T., Matsukawa, Y. Oxide particle-dislocation interaction in 9Cr-ODS steel. *Nuclear Materials and Energy*, (2016) In Press.

86. Hyde, C.J., Sun, W., Hyde, T.H., Saad, A.A. Thermo-mechanical fatigue testing and simulation using a viscoplasticity model for a P91 steel. *Computational Materials Science*, **56** (2012) 29-33.

87. Golden, B.J. University of Limerick, personal communication (2015).

88. Sawada, K., Kushima, H., Tabuchi, M., Kimura, K. Microstructural degradation of Gr.91 steel during creep under low stress. Materials Science and Engineering A, **528** (2011) pp. 5511-5518.

89. Panait, C.G., Bendick, W., Fuchsmann, A., Gourgues-Lorenzon, A.-F., Besson, J. Study of the microstructure of the Grade 91 steel after more than 100,000 h of creep exposure at 600 °C. International Journal of Pressure Vessels and Piping, **87** (2010), pp. 326-335.

90. Li, D.-F., Barrett, R.A., O'Donoghue, P.E., O'Dowd, N.P., Leen, S.B. A multi-scale crystal plasticity model for cyclic plasticity and low-cycle fatigue in a precipitate-strengthened steel at elevated temperature. J. Mechanics and Physics of Solids, (2016) Under Review.

91. Yan, W., Wang, W., Shan, Y.-Y., Yang, K. Microstructural stability of 9-12%Cr ferrite/martensite heat-resistant steels. *Frontiers of Materials Science*, **7** (2013) 1-27.

92. Smallmann, R.E., Bishop, R.J. Modern physical Metallurgy and Materials Engineering. Butterworth-Heinemann: Woburn, MA (1999).

93. Takahashi, Y. Study on creep-fatigue evaluation procedures for high-chromium steels-Part I: Test results and life prediction based on measured stress relaxation. *International Journal of Pressure Vessels and Piping*, **85** (2008) 406-422.